Journal of Materials Chemistry A

ROYAL SOCIETY OF CHEMISTRY

PAPER

View Article Online
View Journal | View Issue

Cite this: J. Mater. Chem. A, 2025, 13, 540

From structure to electrochemistry: the influence of transition metal ordering on Na^+/vacancy orderings in P2-type Na_xMO_2 cathode materials for sodium-ion batteries†

Lukas Fridolin Pfeiffer, ‡*[a] Manuel Dillenz,‡[b] Nora Burgard,[a] Premysl Beran,[cd] Daniel Roscher,[ef] Maider Zarrabeitia,[ef] Paul Drews,[a] Charles Hervoches,[c] Daria Mikhailova,[g] Ahmad Omar,[g] Volodymyr Baran,[h] Neelima Paul,[i] Mohsen Sotoudeh,[b] Michael Busch,[jk] Margret Wohlfahrt-Mehrens,[a] Axel Groß,[b] Stefano Passerini[ef] and Peter Axmann*[a]

P2-type layered oxides are attractive cathode active materials for sodium-ion batteries, however, these materials typically suffer from detrimental Na^+/vacancy orderings. In this work, we investigate the origin as well as the influence of the transition metal ratio on Na^+/vacancy orderings in P2-type cathode materials. A combination of X-ray diffraction (XRD), neutron diffraction, advanced electrochemical methods, *operando* XRD and DFT calculations is applied to study Na^+/vacancy orderings in P2-$Na_xNi_{1/3}Mn_{2/3}O_2$ and P2-$Na_xMn_{3/4}Ni_{1/4}O_2$. In P2-$Na_xNi_{1/3}Mn_{2/3}O_2$, a honeycomb Ni/Mn superstructure leads to charge ordering within the transition metal slab and pronounced Na^+/vacancy orderings, causing distinct voltage jumps at specific sodium contents (x = 2/3, 1/2 and 1/3). For P2-$Na_{0.60}Mn_{3/4}Ni_{1/4}O_2$, the Ni/Mn superstructure is disrupted, resulting in more complex charge orderings within the transition metal slab, partially suppressed Na^+/vacancy orderings and an overall smoother potential profile. Based on our findings, guidelines to suppress Na^+/vacancy orderings in P2-type cathode materials for sodium-ion batteries are postulated and discussed with respect to electrochemical measurements of various transition metal compositions. These guidelines can serve to predict the tendency towards Na^+/vacancy orderings for a given cathode composition or to design new cathode compositions for enhanced cycle life based on the absence of Na^+/vacancy orderings.

Received 10th July 2024
Accepted 15th October 2024

DOI: 10.1039/d4ta04786a

rsc.li/materials-a

Introduction

Increasing energy generation from renewables is inevitable to reduce the impact of man-made climate change.[1] With that, the need for energy storage is gaining importance.[2–4] Today, lithium-ion batteries (LIBs) play a key role in mobile and stationary energy storage,[2,5] however, LIBs contain critical raw materials in terms of availability and cost, such as cobalt, nickel, lithium, copper or graphite.[6–9]

Sodium-ion batteries (SIBs), in which sodium replaces lithium as the ionic charge carrier, are currently being developed and commercialized as a sustainable and potentially cost-effective complementary technology to today's LIBs.[10–13] SIBs typically utilize the same working principle as LIBs,[14] however, critical raw materials are either replaced by more abundant and cost-effective materials or reduced in content.[15,16] On the anode side, hard carbon typically replaces graphite as the active material[17–20] and aluminium is applied as a current collector instead of copper.[15,21,22] As the electrolyte, typically, solutions of $NaPF_6$ in carbonate solvents replace $LiPF_6$ equivalents.[15,23,24] On

[a]ZSW Center for Solar Energy and Hydrogen Research Baden-Württemberg, Helmholtzstraße 8, 89081 Ulm, Germany. E-mail: lukas.pfeiffer@zsw-bw.de; peter.axmann@zsw-bw.de
[b]Institute for Theoretical Chemistry, Mez-Starck-Haus, Oberberghof 7, 89081 Ulm, Germany
[c]Nuclear Physics Institute, CAS, Hlavni 130, 250 68 Rez, Czech Republic
[d]European Spallation Source, ERIC, PO Box 176, 221 00 Lund, Sweden
[e]Helmholtz Institute Ulm, Helmholtzstraße 11, 89081 Ulm, Germany
[f]Karlsruhe Institute of Technology, 76021 Karlsruhe, Germany
[g]Leibniz Institute for Solid State and Materials Research (IFW) Dresden e.V., Helmholtzstr. 20, 01069 Dresden, Germany
[h]Deutsches Elektronen-Synchrotron (DESY), Notkestraße 85, 22607 Hamburg, Germany
[i]Heinz Maier-Leibnitz Zentrum, Technische Universität München, Lichtenbergstraße 1, 85747 Garching, Germany
[j]Division of Materials Science, Department of Engineering Sciences and Mathematics, Luleå University of Technology, 971 87 Luleå, Sweden
[k]Wallenberg Initiative Materials Science for Sustainability (WISE), Luleå University of Technology, 971 87 Luleå, Sweden

† Electronic supplementary information (ESI) available. See DOI: https://doi.org/10.1039/d4ta04786a

‡ Lukas Fridolin Pfeiffer and Manuel Dillenz contributed equally.

the cathode side, sodium-containing intercalation materials substitute lithium nickel cobalt manganese oxides (NCM) or lithium iron phosphate (LFP) as the active material.[10,15,25] Overall, these measures may result in a significantly reduced bill of materials for SIBs and potentially more sustainable batteries.[22,26–30] Additionally, SIBs promise more advantages over today's LIBs in terms of low-temperature performance,[11] power capability,[25] safety, and transportation and storage.[31–33] Furthermore, SIBs can be produced on established production equipment, which reduces necessary investment costs and enables a rapid scale-up of the technology (drop-in technology).[15] Cumulatively, these aspects make SIBs a sustainable and cost-effective secondary battery technology if their performance can be further enhanced.[26]

So far, one of the main bottlenecks for SIBs remains the cathode active material. Currently, mainly three material classes are explored as potential cathode active materials for SIBs, namely Prussian-Blue Analogues (PBAs), sodium vanadium fluorophosphates (NVFP) and layered sodium transition metal oxides (Na_xMO_2).[10,25] Among these three broad families, the latter offers attractive potential and capacity, high (crystal) density and can be produced in a similar fashion as today's NCM for LIBs.[10,25,34–36]

These layered sodium transition metal oxides can be synthesized in an O3, P3 or P2-type structure according to Delmas' notation, where a letter is used as an abbreviation of the alkali metal ion environment (*e.g.*, O = octahedral and P = trigonal prismatic) and a numeral is used to describe the number of transition metal oxygen slabs (MO_2) necessary to describe the unit cell fully. A prime is used to indicate distortion of the ideal structure.[37]

In O3-type layered sodium transition metal oxides, octahedra of adjoining sodium sites share edges. Hence, in these materials the diffusion from one sodium site to another proceeds *via* an intermediate tetrahedral site (divacancy mechanism), leading to moderate Na conductivities.[38,39] In P2-type layered sodium transition metal oxides, prisms of adjoining sodium sites share faces, enabling a single-vacancy mechanism with low activation energy, typically resulting in high diffusion rates.[40] Eventually diffusion rates are a function of the sodium content (vacancy concentration) and can be highly influenced by Na^+/vacancy orderings.[40]

P2-type sodium transition metal oxides typically offer high power capability due to fast solid diffusion, high discharge potential and attractive reversible capacities.[41] In this material class, P2-type $Na_xNi_yMn_{1-y}O_2$ is one of the most investigated sodium layered oxides, due to its attractive performance in terms of reversible capacity and mean discharge potential as well as its high power capability.[10,42]

Synthesis and electrochemistry of P2-$Na_{2/3}Ni_{1/3}Mn_{2/3}O_2$ were first reported by Jeff Dahn and co-workers.[43–45] During reversible electrochemical desodiation at room temperature, P2-$Na_xNi_{1/3}Mn_{2/3}O_2$ follows a solid-solution-like behaviour, maintaining the P2 structure for $x > 1/3$.[44] For $x < 1/3$, a reversible two-phase reaction between P2-$Na_{1/3}Ni_{1/3}Mn_{2/3}O_2$ and O2-$Na_{x\approx 0}Ni_{1/3}Mn_{2/3}O_2$ takes place.[44] The potential profile typically exhibits distinct voltage jumps at sodium stoichiometries of $x = 2/3$, 1/2 and 1/3, which are associated with Na^+/vacancy orderings.[44,46,47] These potential jumps are enclosed by flat regions (indicating the transition between ordered and disordered sodium configurations) at 3.16 V, 3.31 V & 3.56 V and 3.66 V & 4.10 V corresponding to sodium stoichiometries of approximately $x = 2/3 - \delta$, $1/2 \pm \delta$ and $1/3 \pm \delta$ with $0.09 \gtrsim \delta \gtrsim 0.04$, respectively.[44,48–50] The corresponding Na^+/vacancy orderings within the sodium slab have been elucidated using first principles calculations by Meng *et al.*[46] Na^+/vacancy ordered compounds are thermodynamically more stable compared to their disordered counterparts, which results in impeded solid diffusion in proximity to the composition of the ordering[46,51] and potentially limits the cycle life of the battery.[47] Additionally, the potential plateaus caused by Na^+/vacancy ordering are challenging for the application of a battery management system (BMS).[52]

If some of the nickel in P2-$Na_{2/3}Ni_{1/3}Mn_{2/3}O_2$ is substituted by manganese to obtain P2-$Na_{2/3}Mn_{3/4}Ni_{1/4}O_2$, similar performance can be achieved, however, the potential profile is considerably smoother, hinting at largely suppressed Na^+/vacancy orderings.[53–57]

In this work, we investigate the influence of the transition metal ratio on Na^+/vacancy ordering in P2-$Na_xNi_{1/3}Mn_{2/3}O_2$ and P2-$Na_xMn_{3/4}Ni_{1/4}O_2$ cathode active materials for SIBs. Both materials were synthesized and thoroughly characterized, using advanced electrochemical and analytical techniques as well as first principles calculations, to demonstrate that Na^+/vacancy ordering is closely related to charge ordering within the transition metal slab. A general guideline to suppress Na^+/vacancy ordering in P2-type cathode materials is postulated and evaluated against various P2-type sodium transition metal oxides and reports in the literature.

Crystal structure of P2-type $Na_xNi_yMn_{1-y}O_2$

In layered sodium transition metal oxides, transition metals are octahedrally coordinated by oxygen atoms. Edge-sharing MO_6 octahedra form MO_2 slabs. These MO_2 slabs are separated by sodium slabs. Sodium is preferentially located in a triangular prismatic or octahedral environment with six-fold coordination to the surrounding oxygen atoms of the MO_2 slabs.[47] As described above, P2-type Na_xMO_2 structures are characterized by a trigonal prismatic environment of sodium and two MO_2 slabs within the unit cell.[58]

Due to similar X-ray scattering length of 3d transition metals,[59] the crystal structure of P2-type sodium transition metal oxides as derived from X-ray diffraction (XRD) is typically indexed in space group $P6_3/mmc$ (SG 194),[60–62] here noted as a "small unit cell" (Fig. 1A–C). In this structure model, all transition metals are located on the same 2a site, *e.g.*, C, in the hexagonal stacking sequence. Oxygen atoms are located on 4f sites following the ABBA stacking sequence. Sodium ions in the prismatic environment are located either on 2d sites sharing edges with adjacent MO_6 octahedra (Na_e) or 2b sites sharing faces (Na_f) with the adjacent MO_6 octahedra. Please note that

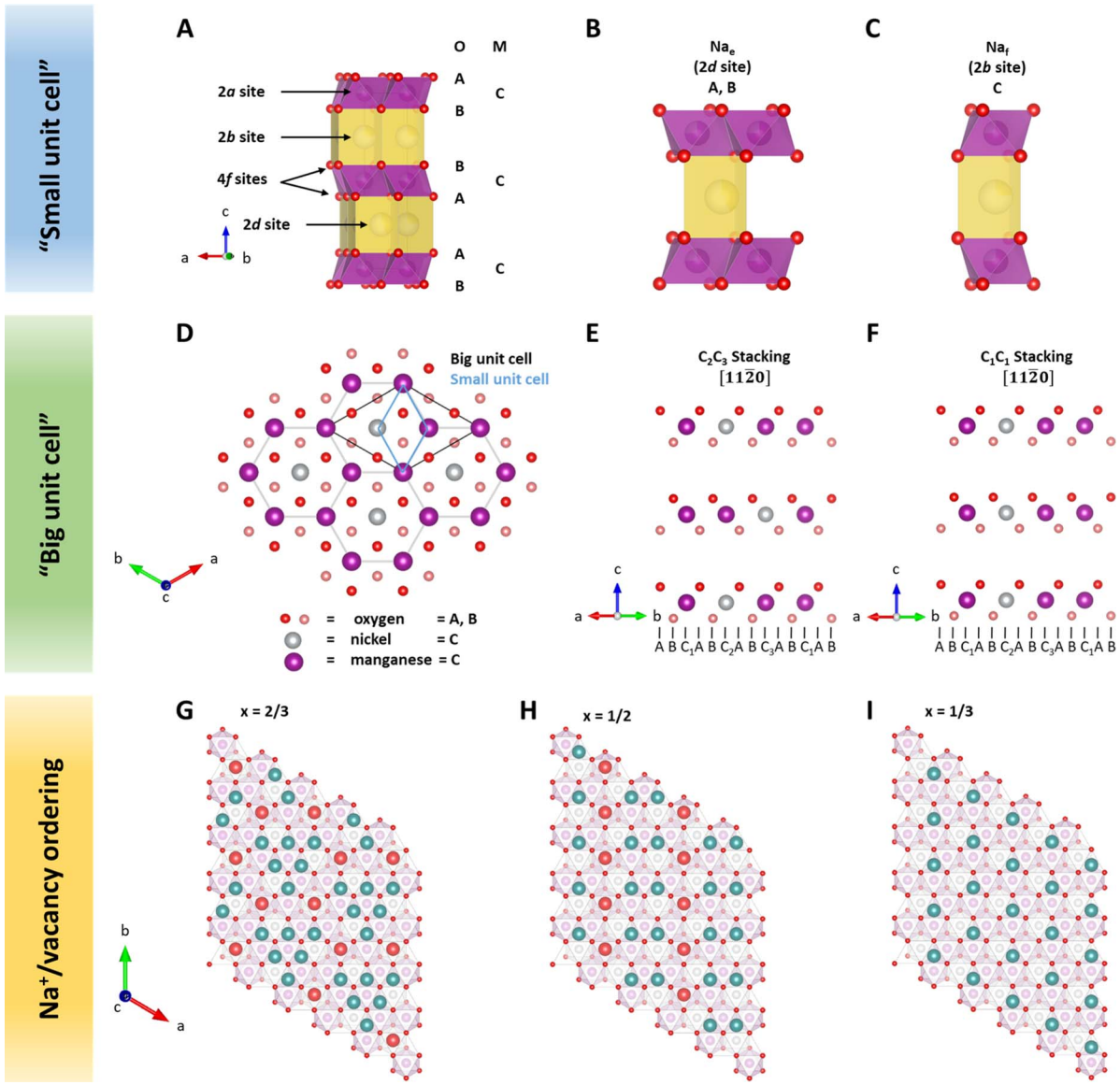

Fig. 1 Schematic representation of the crystal structure of P2-$Na_xNi_{1/3}Mn_{2/3}O_2$ as reported in the literature. (A) Structure of P2-type sodium transition metal layered oxides as described in the small unit cell ($P6_3/mmc$, SG 194), (B) transition metal and oxygen environment for Na_e sites and (C) transition metal and oxygen environment for Na_f sites. (D) Honeycomb Ni/Mn ordering within the MO_2 slab viewed down the [001] direction of the big unit cell (honeycomb transition metal superstructure), (E) C_2C_3 stacking sequence viewed in the [110] direction, and (F) C_1C_1 stacking sequence viewed in the [110] direction. (G) In-plane Na^+/vacancy ordering viewed in the [001] direction at $x = 2/3$, (H) at $x = 1/2$ and (I) at $x = 1/3$. In (G–I) Na_f sites are characteristic of downward facing triangles (▽) and Na_e sites are characteristic of upward facing triangles (△); sodium on Na_f sites is presented in red colour and sodium in Na_e sites is presented in petrol colour.

the number of available sodium sites is twice the amount of transition metal sites. However, the simultaneous occupation of adjacent Na_e and Na_f sites would result in close proximity of sodium ions with shared prismatic faces and is therefore considered unlikely.[63] According to the principles by Linus Pauling, Na_e sites are expected to be energetically more favourable than Na_f sites.[63]

Neutron diffraction (ND) is an invaluable tool for investigating transition metal superstructures due to variant scattering lengths of 3d transition metals.[64] In particular, the neutron scattering length of Mn = −3.73 fm is distinctly different from that of Ni = 10.3 fm. Thus, ND is optimal for identifying sites occupied by these transition metal cations. For P2-$Na_{2/3}Ni_{1/3}Mn_{2/3}O_2$, a honeycomb Ni/Mn ordering within the MO_2 slab is reported, which can be described using a $\sqrt{3}\,a \times \sqrt{3}\,a$ superstructure ($P6_322$, SG 182 or $P6_3$, SG 173),[51,60,65] here noted as a "big unit cell" (Fig. 1D–F). The in-plane honeycomb Ni/Mn ordering together with the small and big unit cells is presented in Fig. 1D. In the big unit cell, three different transition metal sites, C_1, C_2 and C_3, are available, which can be used to describe the stacking sequence of MO_2 slabs in the z-direction. For P2-$Na_{2/3}Ni_{1/3}Mn_{2/3}O_2$, nickel atoms are reported to predominantly occupy alternating C_2 and C_3 sites in stacked MO_2 slabs (C_2C_3 stacking)[60] as presented in Fig. 1E. Interestingly, in the

isovalent P2-$Na_{2/3}Mg_{1/3}Mn_{2/3}O_2$, the same Mg/Mn honeycomb ordering is reported within the MO_2 slab, however, magnesium atoms are predominantly stacked on top of each other following a C_1C_1 stacking sequence ($P6_3/mcm$, SG 193)[60] as presented in Fig. 1F. Simulated ND patterns for the "small unit cell" neglecting any Ni/Mn ordering and the "big unit cell" with Ni/Mn ordering in C_1C_1 and C_2C_3 stacking sequences are presented in ESI Fig. S5.† The simulated diffraction patterns clearly differ between $Q = 1.3$ Å^{-1} and $Q = 2.4$ Å^{-1} due to the presence and stacking sequence of the Ni/Mn honeycomb ordering.

Within the sodium slab, Na^+/vacancy orderings at distinct sodium stoichiometries x are reported[46] (Fig. 1G–I). At $x = 2/3$, sodium ions in Na_f sites arrange in a large-zig-zag (LLZ) around sodium ions in Na_e sites (Fig. 1G). At $x = 1/2$, the ordering can be described as a row of sodium ions in Na_f sites adjacent to two rows of sodium ions in Na_e sites (Fig. 1H). At $x = 1/3$, only Na_e sites are occupied, resulting in an altered row ordering (Fig. 1I). These Na^+/vacancy orderings are accompanied by distinct potential jumps during galvanostatic (de) sodiation.[44,46]

For P2-$Na_xMn_{3/4}Ni_{1/4}O_2$, a similar crystal structure to that in P2-$Na_{2/3}Ni_{1/3}Mn_{2/3}O_2$ with a honeycomb Ni/Mn superstructure in the MO_2 slab is reported, however, with additional manganese atoms located on nickel sites.[54] Based on a smoother potential profile and the absence of Na^+/vacancy superstructure reflections at $x = 0.62$, one report[54] concludes that the LLZ-ordering is disrupted in P2-$Na_{0.62}Mn_{3/4}Ni_{1/4}O_2$.

In this work, we thoroughly characterize the crystal structure of P2-$Na_{2/3}Ni_{1/3}Mn_{2/3}O_2$ and P2-$Na_xMn_{3/4}Ni_{1/4}O_2$ and investigate the extent of Na^+/vacancy ordering and the nature of Na^+/vacancy ordered phases in these materials. Furthermore, this report correlates the in-plane Na^+/vacancy orderings with transition metal charge ordering arising from the transition metal superstructure in these materials.

Experimental

Material synthesis

$Na_{2/3}Ni_{1/3}Mn_{2/3}O_2$, $Na_{2/3}Mn_{3/4}Ni_{1/4}O_2$ and $Na_{0.60}Mn_{3/4}Ni_{1/4}O_2$ were prepared in a three-step synthesis route following co-precipitation of a hydroxide precursor, mixing of the dried precipitate with NaOH as the sodium source and subsequent calcination at high temperature to obtain the final cathode active material (CAM). The dense, spherical $Ni_{1/3}Mn_{2/3}(OH)_2$ and $Mn_{3/4}Ni_{1/4}(OH)_2$ hydroxide precursors were prepared under vigorous stirring in a continuously stirred tank reactor (CSTR, volume = 1 liter). The reactor was constantly fed with deaerated, aqueous solutions of $Mn(NO_3)_2{\cdot}4H_2O$ (Carl Roth) and $Ni(NO_3)_2{\cdot}6H_2O$ (Carl Roth), NH_3 (Carl Roth) and NaOH (Carl Roth). The precipitate collected at the reactor outlet was filtered and washed to remove residual salt solutions and dried. Subsequently, these hydroxide precursors were mixed with respective amounts of aqueous NaOH (Sigma-Aldrich) solution and dried at 80 °C following a wet impregnation procedure. The dried mixture was then calcined in a box furnace (Carbolite Gero). $Na_{2/3}Ni_{1/3}Mn_{2/3}O_2$ was calcined for 10 h at 900 °C in a pure oxygen atmosphere, $Na_{2/3}Mn_{3/4}Ni_{1/4}O_2$ was calcined for 10 h at 900 °C in air as described elsewhere[56] and $Na_{0.60}Mn_{3/4}Ni_{1/4}O_2$ was calcined for 10 h at 1000 °C in pure oxygen. After passive cooling to 200 °C, the powders were directly transferred into a Büchi glass oven, where they were kept at 200 °C under dynamic vacuum overnight. Subsequently, the CAM powders were transferred without any further contact with ambient air into an Ar-filled glovebox (MBraun, H_2O < 0.1 ppm, O_2 < 0.1 ppm). Consecutive powder handling, electrode preparation and cell assembly were conducted in the same glovebox.

For powder characterization with ND, a second batch of $Na_{2/3}Ni_{1/3}Mn_{2/3}O_2$ and $Na_{0.60}Mn_{3/4}Ni_{1/4}O_2$ was prepared based on the same hydroxide precursor and following the same synthesis procedure. A comparison of the characterization results for the two batches is presented in ESI Fig. S6 with ESI Tables S3 and S4 and ESI Fig. S7 with ESI Tables S5 and S6† for $Na_{2/3}Ni_{1/3}Mn_{2/3}O_2$ and $Na_{0.60}Mn_{3/4}Ni_{1/4}O_2$, respectively.

Additionally, P2-$Na_{2/3}Ni_{1/3}Mn_{2/3}O_2$, P2-$Na_{3/4}Ni_{1/4}Li_{1/12}Mn_{2/3}O_2$, P2-$Na_{2/3}Ni_{1/4}Mg_{1/12}Mn_{2/3}O_2$, P2-$Na_{2/3}Ni_{2/9}Al_{1/9}Mn_{2/3}O_2$ and P2-$Na_{2/3}Ni_{1/3}Al_{1/9}Mn_{5/9}O_2$ were synthesized. The respective synthesis route, main characterization results and electrochemical testing procedure are described in the ESI.†

Material characterization

Inductively coupled plasma optical emission spectroscopy (ICP-OES, Spectro Arcos SOP) with a diluted *aqua regia* solution was used for analysis of the chemical composition. Fourier transform infrared spectroscopy in attenuated total reflectance mode (ATR-FTIR) was performed using a Bruker Alpha spectrometer with an Alpha-P ATR unit placed in an Ar-filled glovebox. Scanning electron microscopy (SEM) was used to characterize the powder morphology using a Leo 1530VP (Zeiss) equipped with an Everhart–Thornley SE detector at 5 kV acceleration voltage. Powder XRD patterns were collected on a D8Advance (Bruker) in Bragg–Brentano geometry equipped with a Cu X-ray tube and a LynxEye XE-T detector. Neutron diffraction patterns were recorded at MEREDIT instrument at the Nuclear Physics Institute CAS located in Řež near Prague, Czech Republic. A joint refinement of XRD and ND patterns was performed to obtain lattice parameters, Wyckoff sites and site occupations using the FullProf Suite software.[66] Lattice parameters were refined independently for XRD and ND patterns, due to potentially different measurement temperatures and the different sensitivities of X-ray and neutron radiation. Instrumental broadening was determined from SiO_2 powder on a mosaic Cu(222) monocrystal for ND and NIST640c Si powder for XRD. Based on the results of the joint ND and XRD refinement, FAULTS software[67] was deployed to obtain the stacking probability of P3-type stacking faults from the XRD patterns[56] and to analyse the stacking probability of C_1C_1 stacking faults from ND patterns. The refinement procedure is described in more detail in the ESI.† Throughout the manuscript, depictions of the crystal structures were prepared using VESTA software.[68]

Ex situ capillary transmission XRD measurements were performed on the same D8Advance (Bruker) instrument. For this purpose, CR2032 coin cells were galvanostatically (dis)charged

to obtain the desired active material sodium content and subsequently opened inside an argon filled glovebox. After rinsing with dimethyl carbonate (DMC), the electrode composite was carefully scratched off the aluminium current collector foil and filled into glass capillaries (Ø 0.3 mm, Hilgenberg). The glass capillaries were sealed inside an argon filled glovebox to avoid any contact with the ambient environment.

Electrochemical investigations

Slurries were prepared by homogeneously dispersing a CAM powder, polyvinylidene difluoride binder (PVDF, Solvay Solef 5130) and conductive carbon (SuperP-Li, Imerys Graphite & Carbon) with an 8 : 1 : 1 weight ratio in an appropriate amount of anhydrous *N*-methyl-2-pyrrolidone (Sigma-Aldrich). These slurries were cast on aluminium current collector foils using the doctor blade technique. Electrodes with Ø12 mm and a typical active material mass loading of approximately 4 mg cm^{-2} were punched from the dried electrode sheets. The electrodes were further dried in a Büchi glass oven at 130 °C and dynamic vacuum ($\approx 2 \times 10^{-5}$ bar) overnight. Alumina coated CR2032 coin cells (Hohsen) were prepared using these electrodes, two layers of a glass fibre separator (GFA, Whatman, Ø16 mm), 150 µl of 1 M $NaPF_6$ in propylene carbonate (PC) + 5 wt% fluoroethylene carbonate (FEC) as electrolyte and sodium metal foil as the counter electrode (Acros Organics, Ø16 mm). The galvanostatic intermittent titration technique (GITT) was performed on a VMP3 potentiostat (Biologic) using specific current pulses of 17.3 mA g^{-1} for 10 min within the voltage range of 1.5–4.3 V. Equilibrium was assumed when the absolute voltage change was <0.0001 V h^{-1}. Entropymetry measurements were performed using the same potentiostat and a programmable temperature chamber (CTS GmbH) with temperature steps at 40 °C, 25 °C and 10 °C. Specific current pulses of 8.7 mA g^{-1} with various time periods were applied at 40 °C, followed by a relaxation time of 8 h at the same temperature. In the following, the temperature was changed within 15 min to 25 °C, where it was held for 105 min. Subsequently, the temperature was changed to 10 °C following the same procedure before another current pulse was applied at 40 °C. Equilibrium voltages were derived from the average voltage of the last thirty minutes at each temperature step. The sodium stoichiometry was calculated based on the measured charge of the current pulse and the electrode active material mass, assuming that side reactions were negligible. For every sodium stoichiometry, the entropy change was derived from the obtained slope of the cell voltage with temperature as described in the ESI.†

Operando synchrotron XRD measurements were performed at PETRA III, beamline P02.1 (DESY, Hamburg, Germany).[69] 2D diffraction images were collected using a VATEX CT4343 area detector (2880 × 2880 pixels, 150 × 150 µm pixel size) for 60 seconds. The obtained data were integrated using the DAWN package.[70] An eight-fold coin cell holder, connected to a Biologic Instruments potentiostat, was employed as described elsewhere.[71] A wavelength of 0.20734(1) Å was determined by analysis of the positions of reflections of the LaB_6 reference material (NIST 660C). Prior to recording the first diffraction pattern, the electrochemical cells were subject to a formation cycle at 8.65 mA g^{-1} (discharge to 1.5 V followed by charge to 4.2 V). Subsequently, diffraction patterns were collected with the pre-charged cell by first discharging to 1.5 V followed by charge to 4.3 V at a constant current of 8.65 mA g^{-1}. All diffraction patterns were analysed by the Rietveld method with TOPAS V6 software where the reflections of the Al current collector served as the internal reference.

Throughout this work, either cell voltages from two-electrode measurements with a sodium metal counter electrode or potentials against a sodium metal quasi-reference electrode (three-electrode setup) are reported.

Computational methods

Periodic first-principles calculations based on density functional theory (DFT)[72,73] were performed to determine the convex hull for the Na intercalation for P2-$Na_xNi_{1/3}Mn_{2/3}O_2$ and P2-$Na_xMn_{3/4}Ni_{1/4}O_2$. The projector augmented wave method (PAW)[74] was used in conjunction with the PBE[75] exchange and correlation functional. In addition, the Grimme D3 correction[76] was employed as implemented in the Vienna *Ab initio* Simulation Package (VASP)[77–79] to capture the influence of dispersion effects. The data-driven Hubbard-type *U* corrections[80] of U_{Ni} = 6.2 eV and U_{Mn} = 3.9 eV (ref. 81 and 82) were used to treat the strongly correlated 3d-electrons of the Ni and Mn atoms. The plane wave cut-off was set to 520 eV and a 3 × 3 × 3 *k*-point mesh was employed to sample the Brillouin zone. A large supercell containing 24 formula units and ferromagnetic ordering was chosen. The electronic convergence criterion was set to 1×10^{-6} eV and the structures were relaxed until all forces converged below 0.01 eV $Å^{-1}$. The open circuit potential V_{OCV} in a Na-ion battery is governed by the change in free enthalpy ΔG for the transfer of a Na atom. Thus, the open circuit voltage (OCV) is determined by the difference of the chemical potential μ of Na in the anode and cathode by taking into account the number of transferred electrons n_e and the Faraday constant *F*:

$$V_{OCV} = -\frac{\Delta G}{n_e F} = -\frac{\mu_{cathode} - \mu_{anode}}{n_e F}. \quad (1)$$

By neglecting *pV* and the entropic contributions to ΔG, the difference in the chemical potential of the Na atom is approximated using the total energy of DFT calculations E_{DFT}. The calculation of the V_{OCV} for an exemplary layered oxide compound Na_xMO_2 follows:

$$V_{OCV} = E_{DFT}(Na_{x_1+\Delta x}MO_2) - (E_{DFT}(Na_{x_1}MO_2) + \Delta x E_{DFT}(Na_{metal})). \quad (2)$$

In eqn (2), E_{DFT} is stated in eV and sodium metal is chosen as the reference for the anode. Since the mode of intercalation in these materials deviates from a simple solid-solution behaviour and first order phase transformations at high potentials as well as Na^+/vacancy ordering transitions occur, the convex hull for the Na intercalation compound is derived to identify thermodynamically stable configurations. The convex hull is constructed from the formation energy E_{fx} with respect to the

decomposition into the Na deficient O2-type structure ($x = 0$) and the P2-type structure at a Na content of $x = 2/3$:

$$E_{\mathrm{fx}} = E_x - \frac{x}{\frac{2}{3}}E_{\frac{2}{3}} - \left(1 - \frac{x}{\frac{2}{3}}\right)E_0. \quad (3)$$

Once the convex hull is constructed by calculating the formation energy per formula unit, the OCV for each stable configuration is obtained using eqn (1). The convex hull calculations for P2-$Na_xNi_{1/3}Mn_{2/3}O_2$ and P2-$Na_xMn_{3/4}Ni_{1/4}O_2$ were employed following the previously described procedure for the sodium contents $0 < x < 1/3$ (ref. 53 and 83) and by considering the row and large-zig-zag Na^+/vacancy orderings at the Na contents $x = 1/3$, 1/2 and 2/3 as identified by Lee *et al.*[46] and the alternative Na^+/vacancy ordering at $x = 1/2$ proposed by Huang *et al.*[65,83] Additional Na configurations for the Na contents $x = 1/3$, 5/12, and 7/12 were selected by minimizing the classical Ewald energy[84] assuming integer charges for redox inactive atoms (*i.e.*, Na^+, O^{2-}) and variable charges for the TM atoms (*i.e.*, $Ni^{2+/3+/4+}$, and $Mn^{3+/4+}$) for all possible configurations as implemented in pymatgen.[85] Overall, a minimum of 10 configurations per Na content were obtained for the Na composition range $0 < x < 1/3$ and 20 configurations for the Na composition range $1/3 \leq x \leq 2/3$ in steps of $x = 1/12$ for each compound. Some of the configurations considered in the DFT calculations for $Na_xNi_{1/3}Mn_{2/3}O_2$ are equivalent to the publication by Daubner *et al.*[48]

Results and discussion

Material characterization

The $Na_{2/3}Ni_{1/3}Mn_{2/3}O_2$ and $Na_{0.60}Mn_{3/4}Ni_{1/4}O_2$ cathode active materials were synthesized in our labs, where the reduced sodium content in the latter material is targeted to minimize surface impurities such as NaOH, $NaHCO_3$ or Na_2CO_3.[86,87] For $Na_{2/3}Ni_{1/3}Mn_{2/3}O_2$, a small amount of Na_2CO_3 is detected with ATR-FTIR, whereas the absence of these surface impurities is confirmed for $Na_{0.60}Mn_{3/4}Ni_{1/4}O_2$ by ATR-FTIR measurements as presented together with the reproduced batches in ESI Fig. S8.† Elemental analysis with ICP-OES results in $Na_{0.69}Ni_{0.34}Mn_{0.66}O_2$ and $Na_{0.60}Mn_{0.74}Ni_{0.26}O_2$, respectively, which is in good accordance with the targeted stoichiometries. Based on the knowledge that Mn^{3+}/Mn^{4+} takes place at a lower potential than Ni^{2+}/Ni^{3+} redox,[50,87] we can derive the formal oxidation states $Na_{0.69}Ni_{0.34}{}^{II}Mn_{0.01}{}^{III}Mn_{0.65}{}^{IV}O_2$ and $Na_{0.60}Mn_{0.08}{}^{III}Mn_{0.66}{}^{IV}Ni_{0.26}{}^{II}O_2$, respectively. In both samples, nickel is dominantly divalent and manganese is mainly tetravalent. Particle morphology was characterized using SEM (Fig. 2A–D). Both samples consist of secondary particles with a spherical morphology. The crystal structure was characterized using powder XRD and ND. The diffraction patterns for $Na_{2/3}Ni_{1/3}Mn_{2/3}O_2$ and $Na_{0.60}Mn_{3/4}Ni_{1/4}O_2$ are presented in Fig. 2E–H. For both materials, the obtained XRD pattern (Fig. 2E and F) can be indexed with the hexagonal space group $P6_3/mmc$ (SG 194), indicating phase pure P2-type crystalline structures. For P2-$Na_{2/3}Ni_{1/3}Mn_{2/3}O_2$, the small reflexes located at $Q = 1.9$ Å^{-1} and $Q = 2.0$ Å^{-1} originate from the LLZ Na^+/vacancy ordering (see the inset of Fig. 2E). For P2-$Na_{0.60}Mn_{3/4}Ni_{1/4}O_2$, these superstructure reflexes are absent in accordance with the discrepancy in sodium content (see the inset of Fig. 2F). For P2-$Na_{2/3}Ni_{1/3}Mn_{2/3}O_2$, a subtle split of the (100) and (2$\bar{1}$0) reflections at $Q = 2.5$ Å^{-1} and $Q = 4.3$ Å^{-1} in the XRD pattern suggests a slight orthorhombic distortion of the hexagonal unit cell. Additionally, in both XRD patterns the broadening of (10l) reflections hints at stacking faults. The ND patterns of both samples exhibit reflections between $Q = 1.3$ Å^{-1} and $Q = 2.4$ Å^{-1}, indicating the presence of a Ni/Mn honeycomb ordering with predominantly a C_2C_3 stacking sequence (compare ESI Fig. S5†). Based on these findings, we performed a joint Rietveld refinement of XRD and ND patterns using the "big unit cell" ($P6_322$, SG 182) with a honeycomb Ni/Mn ordering and a C_2C_3 stacking sequence. For P2-$Na_{2/3}Ni_{1/3}Mn_{2/3}O_2$, $C222_1$ (SG 20) was used to account for the slight orthorhombic distortion ($b/a = 1.728$). The results are further refined using "P3-type stacking faults" to account for anisotropic broadening[56] and C_1C_1 stacking faults. The refined lattice parameters, occupancies and staking fault probabilities are summarized in Tables 1 and 2. Both materials, $Na_{2/3}Ni_{1/3}Mn_{2/3}O_2$ and $Na_{0.60}Mn_{3/4}Ni_{1/4}O_2$, exhibit a honeycomb Ni/Mn ordering. For the latter one, this Ni/Mn ordering is partially disrupted as 27% of the nickel site is occupied by manganese. Please note that a different Ni/Mn ordering for the higher Mn content in $Na_{0.60}Mn_{3/4}Ni_{1/4}O_2$ was evaluated, however, the corresponding simulated ND pattern does not match with the experimentally observed one (ESI Fig. S9†). To evaluate any potential influence of the sodium content on the Ni/Mn superstructure, a third sample, $Na_{2/3}Mn_{3/4}Ni_{1/4}O_2$, was synthesized and characterized respectively. The characterization results for $Na_{2/3}Mn_{3/4}Ni_{1/4}O_2$ are presented in ESI Fig. S10 and ESI Table S7.† $Na_{2/3}Mn_{3/4}Ni_{1/4}O_2$ exhibits a similar honeycomb Ni/Mn ordering as $Na_{0.60}Mn_{3/4}Ni_{1/4}O_2$ with approximately one quarter of the nickel site being occupied by manganese in accordance with the stoichiometry. Therefore, no influence of the sodium content on the Ni/Mn superstructure is observed.

Electrochemical characterization

Coin half-cells were assembled using P2-$Na_{2/3}Ni_{1/3}Mn_{2/3}O_2$ or P2-$Na_{0.60}Mn_{3/4}Ni_{1/4}O_2$ as the cathode active material. The galvanostatic intermittent titration technique (GITT) was performed to evaluate the quasi-open circuit voltage (OCV) curve for both materials. The results of the GITT experiments are presented in Fig. 3, where an OCV hull curve is added as a blue line and the on-load hull curve is presented in red colour.

For P2-$Na_xNi_{1/3}Mn_{2/3}O_2$ both the OCV and on-load voltage curves exhibit distinct voltage jumps at $x \approx 2/3$, 1/2 and 1/3 (Fig. 3A). These voltage jumps are accompanied by flat voltage regions as evidenced by the dQ/dV plot (inset of Fig. 3A). In the literature, these voltage jumps are associated with distinct Na^+/vacancy orderings.[44,46] The flat voltage profiles in proximity to these voltage jumps correspond to order/disorder transitions between unordered and Na^+/vacancy ordered phases.[48,83,88–92]

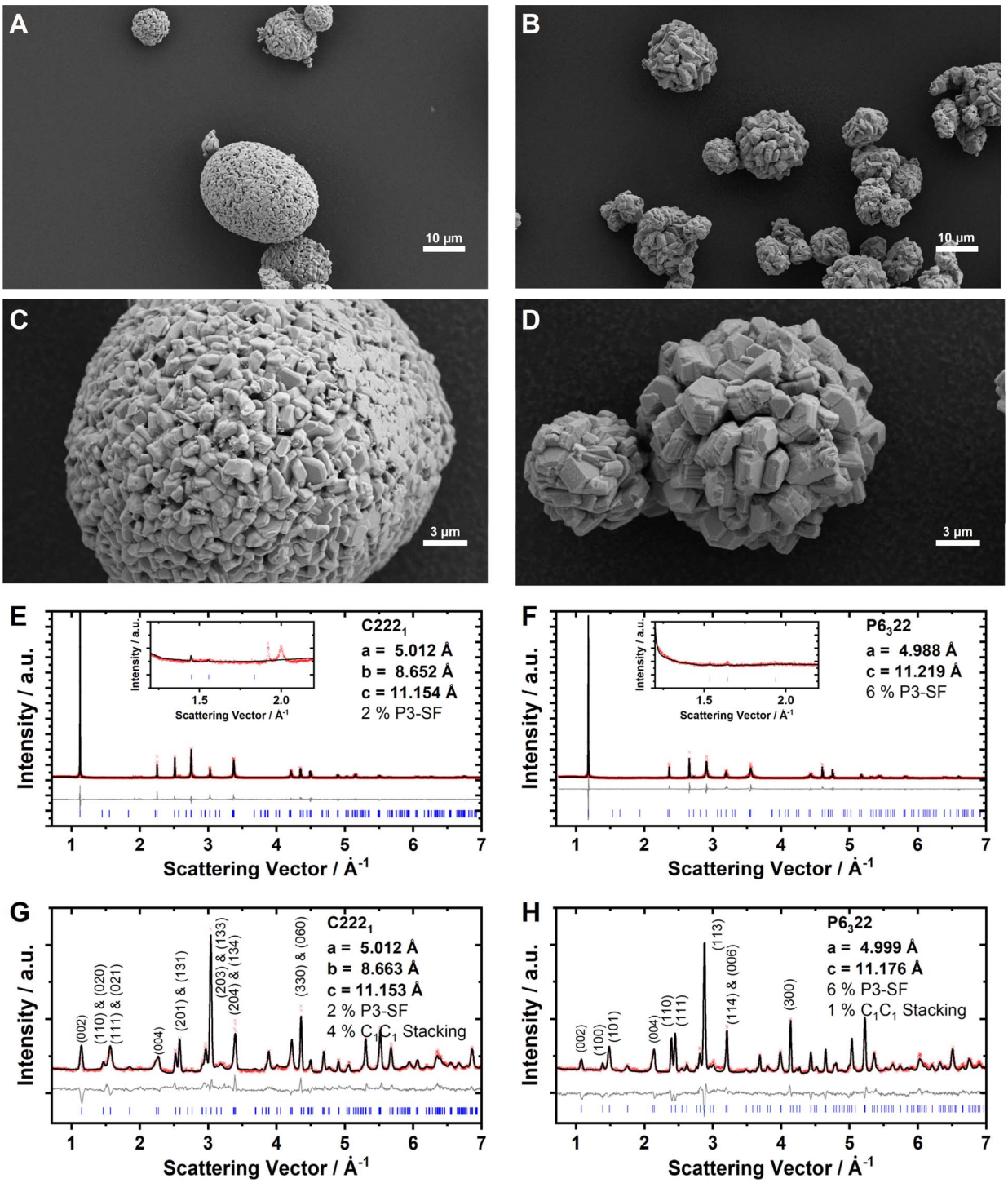

Fig. 2 SEM images of the as-synthesized CAM powders for (A and C) $Na_{2/3}Ni_{1/3}Mn_{2/3}O_2$ and (B and D) $Na_{0.60}Mn_{3/4}Ni_{1/4}O_2$. X-ray diffraction data and Rietveld refinement for (E) $Na_{2/3}Ni_{1/3}Mn_{2/3}O_2$ and (F) $Na_{0.60}Mn_{3/4}Ni_{1/4}O_2$. Neutron diffraction data and Rietveld refinement for (G) $Na_{2/3}Ni_{1/3}Mn_{2/3}O_2$ and (H) $Na_{0.60}Mn_{3/4}Ni_{1/4}O_2$. In (E–H), the measured pattern, the refined pattern, the difference between those two and the position of the Bragg reflections are presented as red crosses, black lines, grey lines and blue bars, respectively.

The voltage profile of P2-$Na_xMn_{3/4}Ni_{1/4}O_2$, – both at equilibrium and under current load – is considerably smoother than those of P2-$Na_xNi_{1/3}Mn_{2/3}O_2$ (Fig. 3A and B). At the same sodium stoichiometries $x = 2/3$, 1/2 and 1/3, the voltage profile exhibits small shoulders in accordance with smaller peaks in the dQ/dV analysis (inset of Fig. 3B).

Whereas the nature of the actual Na^+/vacancy orderings have been reported in the literature for P2-$Na_xNi_{1/3}Mn_{2/3}O_2$, to the best of our knowledge, for P2-$Na_xMn_{3/4}Ni_{1/4}O_2$, the nature of Na^+/vacancy orderings has not been elucidated so far. However, the similarities in composition and structure suggest similar Na^+/vacancy orderings in both materials. The significantly

Table 1 Refined lattice parameters and Wyckoff sites as obtained from a joint refinement of neutron and X-ray diffraction data using FullProf Software and P3-type stacking fault probability as well as C_1C_1-type stacking fault probability as obtained from FAULTS refinement for the sample P2-$Na_{2/3}Ni_{1/3}Mn_{2/3}O_2$. Values for the atomic isotropic displacement parameter B_{iso} were fixed based on the reference[65]

Refinement of ND and XRD patterns using $C222_1$ (SG 20)

ND: $a = 5.0122(3)$ Å, $b = 8.6626(4)$ Å, $c = 11.1248(2)$ Å, $V = 483.030(35)$ Å^3, $R_p = 4.26$, GOF = 2.82
XRD: $a = 5.0115(0)$ Å, $b = 8.6516(0)$ Å, $c = 11.1540(0)$ Å, $V = 483.613(2)$ Å^3, $R_p = 4.40$, GOF = 4.43
P3-type SF: 2.0%, C_1C_1 SF: 4.4%

Atom	x	y	z	Occ	B_{iso}
Na (4*a*)	0	0	0	0	2.526
Na (8*c*)	0	1/3	0.0054(8)	0.2987(63)	2.526
Na (4*a*)	0.3230(8)	0	0	0.6211(18)	2.526
Na (8*c*)	0.1557(6)	0.1557(6)	1/2	0.3657(12)	2.526
Ni (4*a*)	0	0	1/4	0.14	0.276
Mn (4*a*)	0	0	1/4	0.86	0.276
Ni (4*b*)	0	2/3	1/4	0	0.276
Mn (4*b*)	0	2/3	1/4	1	0.276
Ni (4*b*)	0	1/3	1/4	0.92	0.276
Mn (4*b*)	0	1/3	1/4	0.08	0.276
O (8*c*)	0.1744(8)	0.4913(8)	0.8397(6)	1	1.105
O (8*c*)	0.8150(11)	0.1577(9)	0.3427(11)	1	1.105
O (8*c*)	0.1592(10)	0.1682(8)	0.8430(11)	1	1.105

Table 2 Refined lattice parameters and Wyckoff sites as obtained from a joint refinement of neutron and X-ray diffraction data using FullProf Software and P3-type stacking fault probability as well as C_1C_1-type stacking fault probability as obtained from FAULTS refinement for the sample P2-$Na_{0.60}Mn_{3/4}Ni_{1/4}O_2$. Values for the atomic isotropic displacement parameter B_{iso} were fixed based on the reference[65]

Refinement of ND and XRD patterns using $P6_322$ (SG 182)

ND: $a = 4.9989(7)$ Å, $c = 11.1759(27)$ Å, $V = 241.859(77)$ Å^3, $R_p = 5.05$, GOF = 2.95
XRD: $a = 4.9875(1)$ Å, $c = 11.2192(5)$ Å, $V = 241.694(13)$ Å^3, $R_p = 5.35$, GOF = 5.31
P3-type SF: 5.6%, C_1C_1 SF: 0.7%

Atom	x	y	z	Occ	B_{iso}
Na (4*f*)	1/3	2/3	−0.0053(26)	0.2209(36)	2.526
Na (2*a*)	0	0	0	0.2211(35)	2.526
Na (6*g*)	0.3533(3)	0	0	0.3790(12)	2.526
Ni (2*c*)	1/3	2/3	1/4	0.7336(7)	0.276
Mn (2*c*)	1/3	2/3	1/4	0.2664(7)	0.276
Ni (2*d*)	1/3	2/3	3/4	0	0.276
Mn (2*d*)	1/3	2/3	3/4	1	0.276
Ni (2*b*)	0	0	1/4	0	0.276
Mn (2*b*)	0	0	1/4	1	0.276
O (12*i*)	0.3229(8)	0.3339(9)	0.8426(11)	1	1.105

reduced voltage jumps for P2-$Na_xMn_{3/4}Ni_{1/4}O_2$ compared to P2-$Na_xNi_{1/3}Mn_{2/3}O_2$ hint to partially suppressed or disrupted Na^+/vacancy orderings in P2-$Na_xMn_{3/4}Ni_{1/4}O_2$.

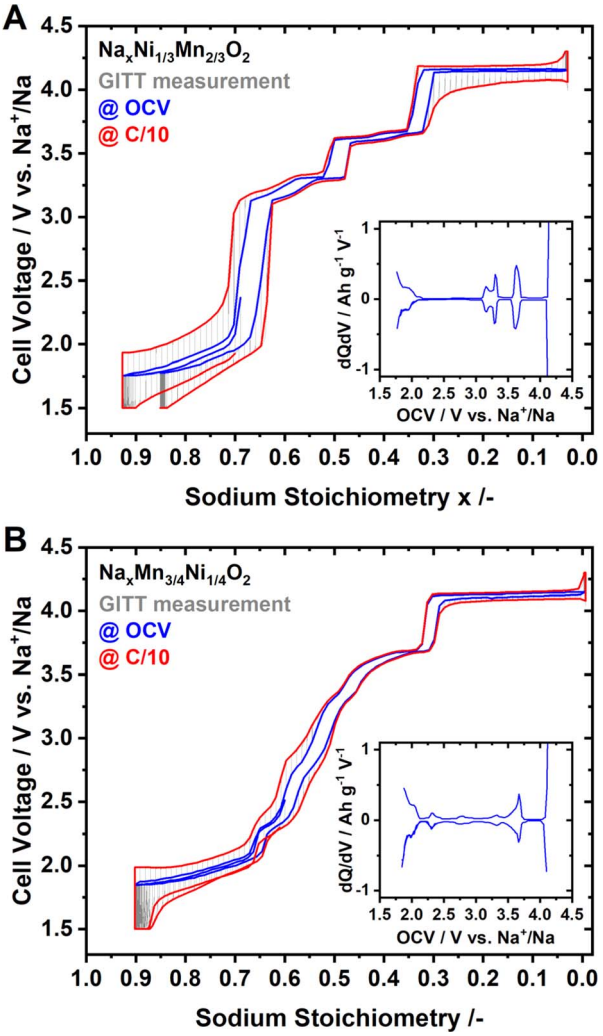

Fig. 3 GITT measurements for (A) $Na_{2/3}Ni_{1/3}Mn_{2/3}O_2$ and (B) $Na_{0.60}Mn_{3/4}Ni_{1/4}O_2$ as CAM. The OCV for various stoichiometries is highlighted as a blue hull curve, and the on-load hull curve is highlighted in red colour. For both materials, dQ/dV analysis of the OCV curve is included in the inset.

To further investigate the nature and extent of Na^+/vacancy orderings in both materials, synchrotron *operando* XRD measurements were performed. Waterfall diagrams of the obtained diffraction patterns are presented in Fig. 4A and B for P2-$Na_xNi_{1/3}Mn_{2/3}O_2$ and P2-$Na_xMn_{3/4}Ni_{1/4}O_2$, respectively. For both materials, the measurements start with sodiation from the charged state. The diffraction patterns corresponding to sodium contents of $x = 2/3$, 1/2 and 1/3 are highlighted in red, magenta and green colour, respectively. For P2-$Na_xNi_{1/3}Mn_{2/3}O_2$, clear superstructure reflections in proximity to the sodium content of $x = 2/3$, 1/2 and 1/3 are apparent. Simulated diffraction patterns based on the reported in-plane Na^+/vacancy ordering by Lee *et al.*[46] and Huang *et al.*[83] are presented in ESI Fig. S11,† in which the range of experimentally found superstructure reflections is highlighted in yellow colour for the ease of comparison. At sodium stoichiometries of $x = 2/3$ and 1/3, the observed superstructure reflexions match the simulated pattern based on the

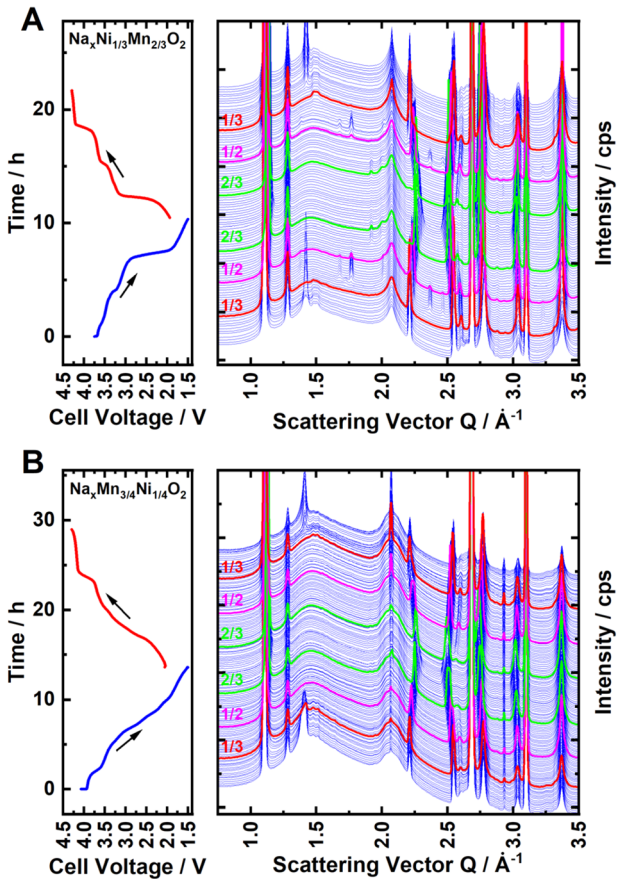

Fig. 4 Synchrotron *operando* XRD for (A) $Na_{2/3}Ni_{1/3}Mn_{2/3}O_2$ and (B) $Na_{0.60}Mn_{3/4}Ni_{1/4}O_2$. Both measurements were started in a charged state. The diffraction patterns corresponding to sodium stoichiometries of $x = 1/3$, 1/2 and 2/3 are highlighted in red, magenta and green colour, respectively.

Na^+/vacancy ordering reported by Lee *et al.*[46] For $x = 1/2$, observed superstructure reflections match the report by Huang *et al.*[83] in accordance with a previous publication.[65]

For P2-$Na_xMn_{3/4}Ni_{1/4}O_2$, similar superstructure reflections in proximity to $x = 2/3$ and 1/3 are apparent, however, the superstructure reflection at $x = 2/3$ is very weak. For P2-$Na_{1/2\pm\delta}Mn_{3/4}Ni_{1/4}O_2$, no superstructure reflection is observed, indicating that no long-range Na^+/vacancy ordering exists at this stoichiometry. The comparably low intensity of the Na^+/vacancy superstructure reflection in P2-$Na_xMn_{3/4}Ni_{1/4}O_2$ is indicative of either decreased long-range order (disrupted ordering) or a smaller weight fraction of the ordered phase (partial ordering). For both materials, the similarity of the superstructure reflection at $x = 2/3$ and 1/3 supports the assumption that the in-plane Na^+/vacancy ordering is the same for both materials. These observations are in accordance with diffraction patterns obtained by *ex situ* capillary transmission XRD, as presented in ESI Fig. S12.† For both materials, the heat maps of the obtained diffraction patterns as well as the refined lattice parameters (Pawley method) are presented in ESI Fig. S13 and S14.† A good agreement of refined lattice parameters as well as the nature and extent of the detected Na^+/vacancy ordering is found for synchrotron *operando* XRD and *ex situ* capillary transmission XRD, indicating that the *operando* measurement is close to equilibrium.

To measure the extent of Na^+/vacancy orderings at various stoichiometries, entropymetry measurements were performed. A detailed description of the method is provided in the ESI.† In short, the equilibrium voltage at different sodium contents was measured at 40 °C, 25 °C and 10 °C following a GITT procedure including temperature change at every equilibrium step. The change in measured equilibrium voltage E_{OCV} with the change in temperature ΔT is proportional to the entropy change ΔS at the corresponding sodium content x, according to:

$$\Delta S(x) = nF\left.\frac{E_{OCV}}{\Delta T}\right|_{x=\text{const}}$$

Several factors, such as the configurational entropy, phonon entropy and electronic entropy, can contribute to the entropy change of a material.[93] However, the course of the entropy change is reported to be highly dominated by the configurational entropy,[93] making entropymetry a valuable tool to investigate it.

The entropy change derived from several independent cells is presented in Fig. 5A and B for P2-$Na_xNi_{1/3}Mn_{2/3}O_2$ and P2-$Na_xMn_{3/4}Ni_{1/4}O_2$, respectively. For P2-$Na_xNi_{1/3}Mn_{2/3}O_2$, the entropy change curve exhibits a distinct double-S shape in proximity to sodium contents $x \approx 2/3$, 1/2 and 1/3. As described in the ESI,† such a double-S shaped course of the entropy change is expected in proximity to Na^+/vacancy ordered phases. For P2-$Na_xMn_{3/4}Ni_{1/4}O_2$, the entropy change curve follows a double-S shape at $x \approx 2/3$, 0.54, 1/2 and 1/3, indicative of Na^+/vacancy ordering at these stoichiometries. For P2-$Na_xMn_{3/4}Ni_{1/4}O_2$, the variation of entropy change at $x \approx 2/3$ and 1/2 is significantly smaller compared to P2-$Na_xNi_{1/3}Mn_{2/3}O_2$, indicating a reduced extent of Na^+/vacancy orderings in the former material. The double-S shaped course of the entropy change in proximity to $x \approx 0.54$ might correspond to a weak Na^+/vacancy ordering resembling the reported Na^+/vacancy ordering in $Na_{4/7}CoO_2$.[90,92,94] We have estimated the expected potential jump based on the measured configurational entropy change and summarized the estimated potential differences due to Na^+/vacancy orderings in ESI Table S8.† The results further corroborate more pronounced Na^+/vacancy orderings at $x = 2/3$ and 1/2 for P2-$Na_xNi_{1/3}Mn_{2/3}O_2$ compared to P2-$Na_xMn_{3/4}Ni_{1/4}O_2$. Furthermore, the measured voltage jumps in GITT measurements (Fig. 3) at $x = 2/3$, 1/3 in P2-$Na_xNi_{1/3}Mn_{2/3}O_2$ and at $x = 1/3$ in P2-$Na_xMn_{3/4}Ni_{1/4}O_2$ significantly exceed the estimated potential jumps due to configurational entropy change (*i.e.*, Na^+/vacancy ordering), suggesting additional processes contributing to these voltage jumps. For $x = 2/3$ in P2-$Na_xNi_{1/3}Mn_{2/3}O_2$, the energy difference between $Ni^{2+/3+}$ redox and $Mn^{3+/4+}$ redox is expected to significantly contribute to the voltage jump at $x = 2/3$ in P2-$Na_xNi_{1/3}Mn_{2/3}O_2$. For both materials, the onset of the P2–O2 phase transition is expected to contribute to the voltage jump at $x = 1/3$.

Overall, GITT, *operando* XRD, *ex situ* XRD, and entropymetry indicate similar Na^+/vacancy orderings at $x = 2/3$ and 1/3 in P2-$Na_xNi_{1/3}Mn_{2/3}O_2$ and P2-$Na_xMn_{3/4}Ni_{1/4}O_2$. For $x = 2/3$ and $x =$

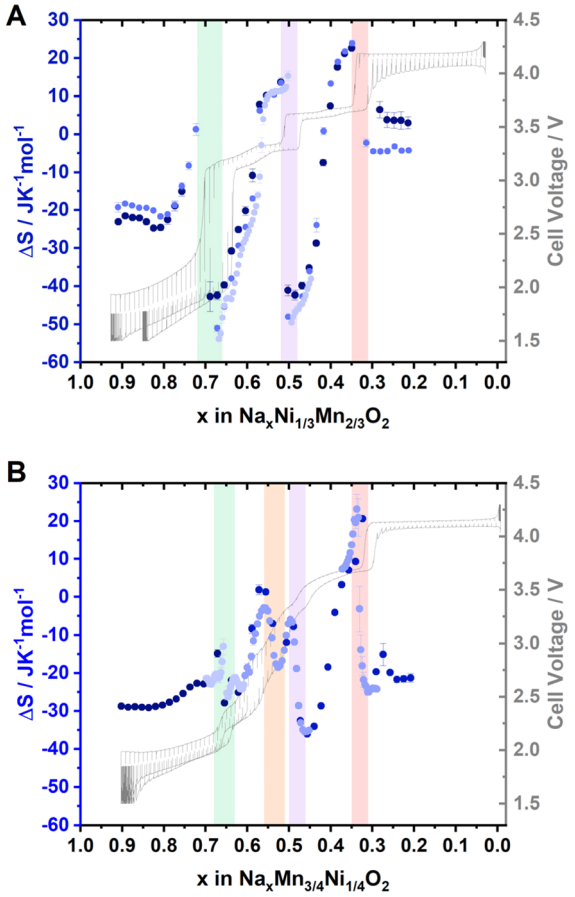

Fig. 5 Entropymetry measurements for (A) $Na_{2/3}Ni_{1/3}Mn_{2/3}O_2$ and (B) $Na_{0.60}Mn_{3/4}Ni_{1/4}O_2$. A detailed description of the method is provided in the ESI.† Jumps in the entropy change indicative of Na^+/vacancy ordering are highlighted with coloured background. A GITT measurement is provided in grey colour in the background. For both materials, the results from independent cells are presented in different colour. The uncertainty of the linear regression is presented as error bars.

1/2, XRD and entropymetry measurements suggest a disrupted Na^+/vacancy ordering in P2-$Na_xMn_{3/4}Ni_{1/4}O_2$. For $x = 1/3$, no significant influence of the Ni/Mn ratio on the Na^+/vacancy ordering is detected.

In general, Na^+/vacancy orderings in these structures result from the high stability (low Gibbs free enthalpy) of the ordered configurations. In Na^+/vacancy ordered phases, Gibbs free enthalpy is eventually reduced by (i) minimized Na^+–Na^+ repulsion within the sodium layer and (ii) advantageous interaction of Na^+ with the immediate environment of the MO_2 slab (*i.e.*, low energy sodium lattice sites). For the herein investigated materials, the transition metals, nickel and manganese, are known to adopt different formal oxidation states depending on the applied electrode potential.[50,87] Hence, the stability of sodium sites is eventually influenced by the transition metals in the immediate environment and the formal oxidation states thereof. The resulting difference in energy for various sodium sites potentially contributes to the preferential occupation of these sites (*i.e.*, preferential occupation of low-energy sodium sites).

Computational

Computational methods were employed to gain further insights into the origin of Na^+/vacancy orderings in P2-$Na_xNi_{1/3}Mn_{2/3}O_2$ and P2-$Na_xMn_{3/4}Ni_{1/4}O_2$. First, we identify the thermodynamically stable phases. Then, we evaluate the electronic structure and the charge density distribution of the transition metals in these materials. Subsequently, we evaluate the existence of low-energy sodium lattice sites in the absence of Na^+–Na^+ repulsion. Finally, we analyse the charge ordering within the MO_2 slab and correlate these findings with the existence and stability of Na^+/vacancy orderings.

Spin polarized periodic DFT calculations were performed to determine the thermodynamically stable phases and construct the convex hull for P2-$Na_xNi_{1/3}Mn_{2/3}O_2$ and P2-$Na_xMn_{3/4}Ni_{1/4}O_2$. For P2-$Na_xNi_{1/3}Mn_{2/3}O_2$, the implemented unit cell includes 24 transition metal atoms arranged in a characteristic honeycomb Ni/Mn ordering in accordance with our characterization results and the literature[60] (Fig. 6A). By substituting every fourth Ni by Mn, the unit cell for P2-$Na_xMn_{3/4}Ni_{1/4}O_2$ with a defect honeycomb transition metal ordering is obtained according to the characterization results (Fig. 6B). Even though the in-plane sodium arrangement has been reported for the Na^+/vacancy orderings at $x = 2/3$, 1/2 and 1/3 in P2-$Na_xNi_{1/3}Mn_{2/3}O_2$,[46] to the best of our knowledge, the relation of this in-plane sodium ordering to the honeycomb ordered MO_2 slabs has not been analysed so far. To fill this gap, we have calculated the free enthalpy for the reported in-plane sodium vacancy orderings at various sites in these large Ni/Mn ordered superstructure cells. The calculated convex hull is presented in Fig. 6C and D for P2-$Na_xNi_{1/3}Mn_{2/3}O_2$ and P2-$Na_xMn_{3/4}Ni_{1/4}O_2$, respectively. For P2-$Na_xNi_{1/3}Mn_{2/3}O_2$, solely the O2-structure at $x = 0$ and the Na^+/vacancy ordered P2-structures at $x = 1/3$, 1/2 and 2/3 are located on the convex hull. At $x = 1/2$, the Na^+/vacancy ordering, as reported by Huang *et al.*,[83] was calculated to be energetically favourable, which is in accordance with our *operando* XRD results and literature reports for $Na_{1/2}CoO_2$.[90,91,95–99] At $x = 2/3$, the determined stable structure exhibits the same in-plane Na^+/vacancy ordering;[98,99] however, the stacking sequence differs from reports on P2-$Na_{2/3}CoO_2$.[90,100,101] For P2-$Na_xMn_{3/4}Ni_{1/4}O_2$, the O2-structure at $x = 0$ and the P2-structures at $x = 1/3$, 5/12, 1/2, 7/12 and 2/3 are located on the convex hull. At $x = 1/2$, the reported ordering by Lee *et al.*[46] was calculated to be slightly more stable than the ordering reported by Huang *et al.*[83] The marginal difference in energy between both orderings is in accordance with the disrupted Na^+/vacancy ordering observed with *operando* XRD and entropymetry measurements.

In general, configurations located on the convex hull (Fig. 6C and D) are stable, whereas all configurations with formation enthalpies above the convex hull are unstable or metastable. The convex hull directly relates to the enthalpy difference between sodium in intercalated and metallic form, whereas the measured OCV curve, as presented in Fig. 3, represents the Gibb's free energy (enthalpic plus entropic contribution) of the

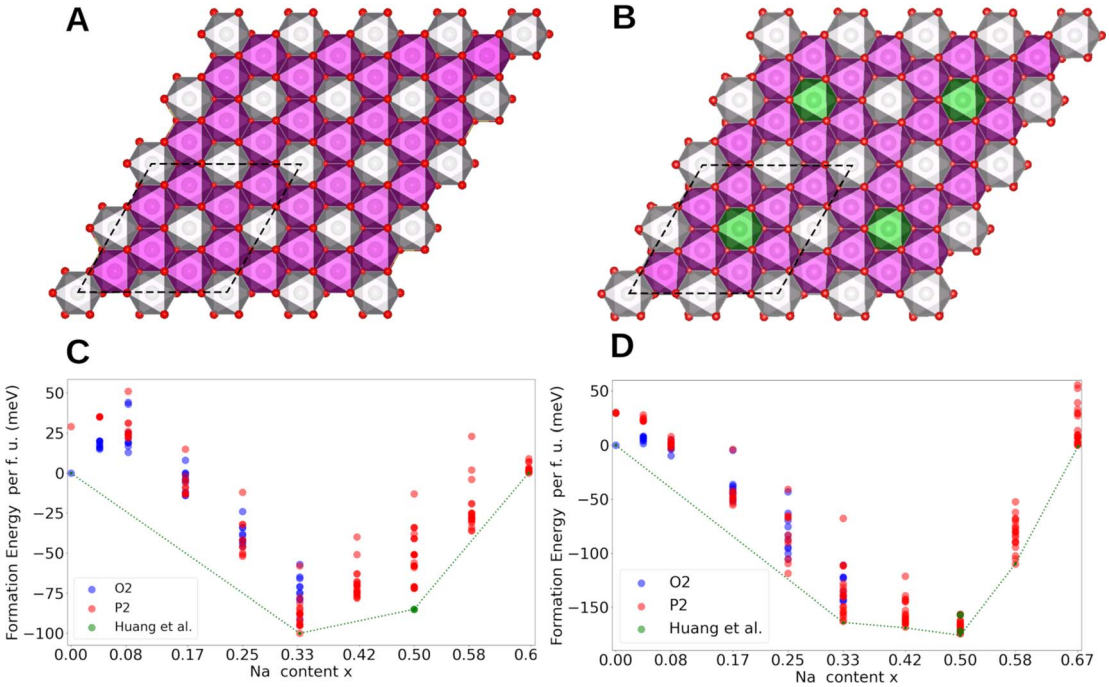

Fig. 6 Honeycomb transition metal ordering in (A) P2-$Na_{2/3}Ni_{1/3}Mn_{2/3}O_2$ and in (B) P2-$Na_{2/3}Mn_{3/4}Ni_{1/4}O_2$ and the corresponding convex hull for the Na intercalation for (C) P2-$Na_{2/3}Ni_{1/3}Mn_{2/3}O_2$ and (D) P2-$Na_{2/3}Mn_{3/4}Ni_{1/4}O_2$. The Ni atoms are coloured in grey, Mn atoms in magenta, and O atoms in red. The additional Mn atoms located on Ni sites in (B) are highlighted in green. In (A and B), the supercell employed in the DFT calculations is shown in black. In (C and D), the formation energy per formula unit for Na configurations in the P2 structures and the O_2 structures are shown in red and blue, respectively.

same reaction. In the convex hull, segments of solely unstable configurations (*e.g.*, $0 < x < 1/3$ in P2-$Na_xNi_{1/3}Mn_{2/3}O_2$) represent a miscibility gap between the respective stable endmembers (*e.g.*, O2-$Na_0Ni_{1/3}Mn_{2/3}O_2$ and P2-$Na_{1/3}Ni_{1/3}Mn_{2/3}O_2$). The corresponding two-phase reaction results in a characteristic voltage plateau in the electrochemical potential profile.[102] Overall, the calculated convex hull well describes the course of the experimentally determined OCV curve, suggesting that the enthalpy change dominates the course of the Gibb's free energy, however, small differences between the convex hull and the experimentally derived OCV curve exist. For P2-$Na_xNi_{1/3}Mn_{2/3}O_2$ (Fig. 6C), the miscibility gap in the ranges $1/3 < x < 1/2$ and $1/2 < x < 2/3$ is expected to cause a voltage plateau. Experimentally, we find two small voltage plateaus associated with the order/disorder transitions in proximity to the respective Na^+/vacancy orderings and observe distinct voltage jumps for Na^+/vacancy ordered phases. The difference between the expected potential profile based on the convex hull and the measured voltage profile eventually arises from (finite) temperature effects. For P2-$Na_xMn_{3/4}Ni_{1/4}O_2$ (Fig. 6D), no miscibility gap is expected between $1/3 < x < 2/3$ based on the convex hull in line with the much smoother electrochemical voltage profile in Fig. 3B.

To elucidate the nature of the M–O and Na–O bonds, Density Overlap Regions Indicators (DORI)[103] were determined for P2-$Na_{2/3}Ni_{1/3}Mn_{2/3}O_2$ as presented in Fig. 7. The DORI analysis was developed to distinguish covalent from noncovalent interactions, while differences between metallic and ionic bonding cannot be resolved. In this framework, covalent interactions are revealed by localized overlap indicators, while noncovalent interactions are characterized by fully smeared out overlap indicators. This analysis is not restricted to interactions in molecules as similar bonding characteristics exist in solids and DORI was already successfully applied to Mn-oxides.[104]

Hence, the DORI analysis in Fig. 7 allows tracking qualitative differences in bonding character between the different bonds in the system. Qualitatively identical results were observed independent of Na content and the Ni/Mn ratio and are depicted in ESI Fig. S15.† While the Mn–O and Ni–O bonds are characterized by localized basins of DORI values close to 1, indicating increased covalent character, the Na–O bonds show entirely

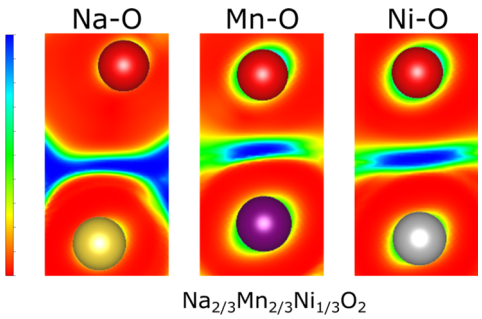

Fig. 7 The DORI of the Na–O bond, the Mn–O bond, and the Ni–O bond in P2-$Na_{2/3}Ni_{1/3}Mn_{2/3}O_2$. DORI values of 1 imply overlapping density regions and are shown in blue while DORI values of 0 are shown in red.

smeared out overlap indicators implying ionic bonding. The revealed covalent nature of the M–O bond is in good agreement with what has been found for many other comparable oxides[104,105] and corresponds to a distribution of the electron density along the M–O bond. Thus, only formal oxidation states, which do not necessarily agree with the true charge at the ion, can be assigned. This observation is in accordance with the calculated Bader charges, which indicate lower electron density at the transition metal ion than that suggested by the formal oxidation state (see Table 3).

To further elucidate the nature of the M–O bonding, we determined the partial density of states (PDOS) shown in Fig. 8A. Indeed, no Na 2s states are found in the valence band region in agreement with the ionic character of the Na–O bond. In contrast, the M-3d states are found to strongly hybridise with the O-2sp^3 states in the valence band region, possibly indicating the prevalence of covalent bonding in the MO_2 layer. While this supports the simplified picture of the Na atoms donating their electrons to the MO_2 layer, it raises the question of the charge density distribution in the MO_2 slab. Specifically, it is of interest whether electrons (e^-) are entirely localized in M–O bonds or whether they are delocalized over several transition metal atoms. In fact, transition metal compounds are well known to delocalize electrons through direct exchange or super exchange interactions.[106] In the present case, however, no direct overlap between metal 3d orbitals are possible owing to the long metal–metal distance and the ferromagnetic coupling between ions. Instead, delocalisation is achieved through a super-exchange interaction whereby electrons are delocalized through an at least partially covalent M–O–M two electron three center (2e3c) bond. This is a well known bonding scheme in inorganic chemistry[106,107] which has also been observed for related compounds such as manganese hydroxo complexes[108] and Cu_2O.[105,109] These observations suggest that similar bonding characteristics can possibly lead to delocalization of e^- also in the here investigated samples.

For P2-$Na_xNi_{1/3}Mn_{2/3}O_2$ (Fig. 8A), independent of Na content, the low spin Ni t_{2g} orbitals are fully occupied in both spin majority and minority directions and are found in the range from −6 eV to 0 eV. The Ni e_g^* orbitals are either empty ($x = 0$) and form the conduction band or are partially occupied ($x > 0$) and situated below the Fermi level, depending on the Na content in the structure. During sodiation of $Na_xNi_{1/3}Mn_{2/3}O_2$, first the low lying Ni e_g^* are partially occupied and shifted below the Fermi energy. At a sodium content of $x = 1/3$ the Ni atoms are formally Ni^{3+} and undergo a Jahn–Teller splitting of the e_g^* into occupied $d_{x^2-y^2}$ and unoccupied d_{z^2} states (Fig. 8B). This is followed by further reduction of Ni from Ni^{3+} to Ni^{2+} with increasing Na content leading to fully occupied Ni e_g^* states at a Na content of $x = 2/3$. Independent of the sodium content x ($2/3 > x > 0$), Mn t_{2g} orbitals are fully occupied in the spin majority direction and empty in the spin minority direction and are found in the range between −6 eV and 0 eV. The Mn e_g^* orbitals are situated between 1.5 eV and 2.5 eV independent of the Na content x and hence do not contribute to the electrochemical processes in this material ($0 < x < 2/3$). The significant potential jump at $x = 2/3$, as observed in GITT measurements (Fig. 3), is qualitatively supported by the observed energy difference between Ni e_g^* and Mn e_g^* states in PDOS.

In P2-$Na_xMn_{3/4}Ni_{1/4}O_2$, PDOS features appear similar, however, they are shifted in sodium content. Due to the reduced Ni content in $Na_xMn_{3/4}Ni_{1/4}O_2$, the respective Ni redox processes are shifted to lower Na contents and Ni e_g^* is fully occupied at $x = 1/2$. For $x = 2/3$, the Mn e_g^* orbitals are partially occupied and shifted below the Fermi level. With increasing sodium content, the continuously increasing occupation of the Ni e_g^* and Mn e_g^* can be rationalized considering octahedral crystal field splitting (Fig. 8B) in conjunction with the formal oxidation states of the transition metal centre. Thus, sodiation beyond $x = 1/2$ leads to Mn redox activity and the formation of Jahn–Teller active Mn^{3+} by partial occupation of Mn e_g^* states.

To corroborate the observations in the PDOS, we have analysed local magnetic moments μ and Bader charges of the transition metal atoms and summarized the results in Table 3. The local magnetic moment allows distinguishing between transition metals of different formal oxidation states based on

Table 3 The average local magnetic moment μ and the Bader charge of Mn and Ni for the lowest energy structures in P2-$Na_xNi_{1/3}Mn_{2/3}O_2$ and P2-$Na_xMn_{3/4}Ni_{1/4}O_2$ for the Na contents $x = 1/3$, 1/2 and 2/3. The local magnetic moments constitute averages over all Ni and Mn atoms with the same formal oxidation state (OS) and variations were found to be negligible. Local magnetic moments and Bader charges associated with different oxidation states are separated by semicolons. At $x = 0$ both materials adopt the O2-structure

	Mn			Ni		
Na content x	μ [μ_B]	Bader [e$^-$]	OS	μ [μ_B]	Bader [e$^-$]	OS
$Na_xNi_{1/3}Mn_{2/3}O_2$						
1/3	3.19	1.84	4+	1.20	1.32	3+
1/2 (Lee)[46]	3.18	1.84	4+	1.18; 1.73	1.21; 1.31	2+; 3+
1/2 (Huang)[83]	3.18	1.84	4+	1.18; 1.76	1.21; 1.31	2+; 3+
2/3	3.19	1.84	4+	1.76	1.20	2+
$Na_xMn_{3/4}Ni_{1/4}O_2$						
1/3	3.21	1.84	4+	1.19; 1.76	1.22; 1.36	2+; 3+
1/2 (Lee)[46]	3.19	1.84	4+	1.76	1.21	2+
1/2 (Huang)[83]	3.19	1.84	4+	1.76	1.21	2+
2/3	3.21; 3.86	1.70; 1.83	3+; 4+	1.76	1.21	2+

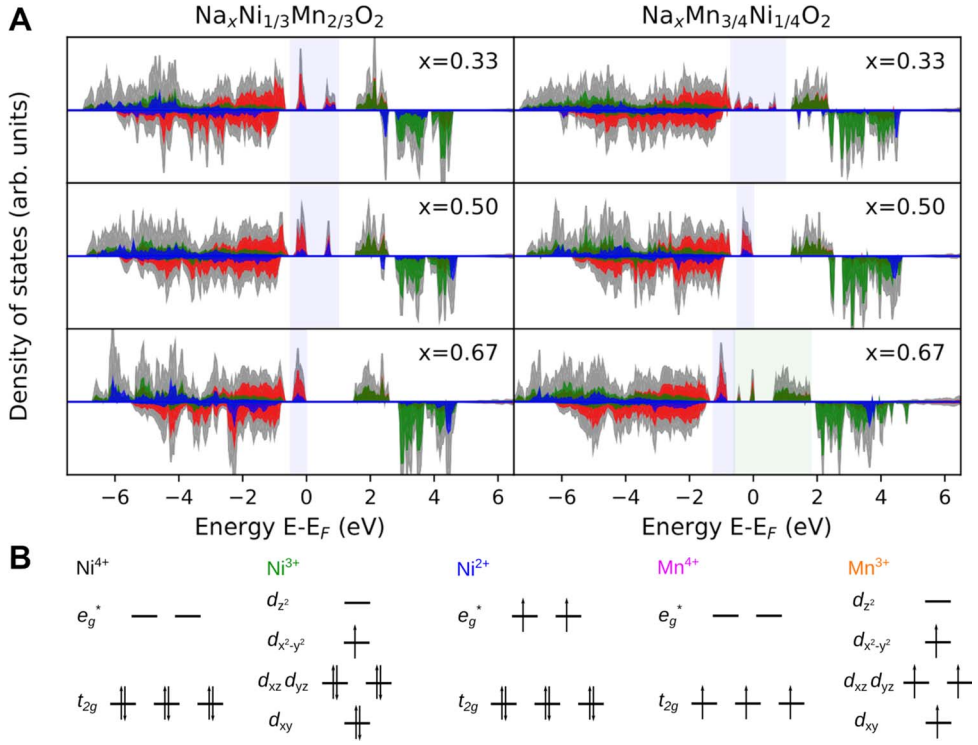

Fig. 8 (A) The PDOS for the Na contents $x = 1/3$, 1/2, and 2/3 in P2-$Na_xNi_{1/3}Mn_{2/3}O_2$ and P2-$Na_xMn_{3/4}Ni_{1/4}O_2$. The Ni e_g^* and Mn e_g^* are highlighted in blue and green background colour, respectively. DOS for Mn, Ni and O are depicted in green, blue and red colour, respectively. Total DOS are presented in grey colour. (B) The octahedral crystal field splitting for the transition metal atoms in various formal oxidation states accounting for the Jahn–Teller distortion of Ni^{3+} and Mn^{3+}.

the number of unpaired electrons expected from the crystal field splitting as presented in Fig. 8B. In contrast, Bader charges are determined by charge partitioning of the charge density obtained using DFT and yield qualitative trends for charge situated at the transition metal centre. Despite their fundamentally different methodologies, both methods show similar trends in agreement with the analysis of the PDOS.

For P2-$Na_xNi_{1/3}Mn_{2/3}O_2$, with increasing sodium content, the local magnetic moment increases and Bader charges decrease for Ni, whereas both values remain invariant for Mn. Hence, with increasing sodium content, Ni is gradually reduced from Ni^{3+} at $x = 1/3$ to Ni^{2+} at $x = 2/3$, while Mn is redox inactive. At $x = 1/2$, Ni^{3+} and Ni^{2+} are detected in equal amounts.

For P2-$Ni_xMn_{3/4}Ni_{1/4}O_2$, with increasing sodium content, the local magnetic moment increases and the Bader charges decrease for Ni from $x = 1/3$ to $x = 1/2$, whereas Mn remains invariant within this sodium range. Further sodiation from $x = 1/2$ to $x = 2/3$, leads to increasing local magnetic moment and decreasing Bader charges for Mn, whereas Ni is invariant. Hence, Ni is redox active for $x < 1/2$ and Mn is redox active at sodium contents $x > 1/2$.

Overall, the analysis of PDOS, the local magnetic moment μ and Bader charges, suggest that charge within the MO_2 slab is considerably localized at the covalently bonded transition metals, making formal oxidation states an acceptable descriptor for P2-$Na_xNi_{1/3}Mn_{2/3}O_2$ and P2-$Ni_xMn_{3/4}Ni_{1/4}O_2$. Please note that similar charge disproportionation has been reported for P2-Na_xCoO_2 and O′3-Na_xMnO_2 with experimental and computational methods.[83,95–97,110–112]

As described above, various transition metal oxidation states within the MO_2 slab potentially result in low energy sodium sites. The interplay between the preferential occupation of these low energy sodium sites and Na^+–Na^+ repulsion eventually results in Na^+/vacancy orderings. To deconvolute these two effects, we have calculated sodium site energies at a high vacancy limit by placing one sodium atom in a supercell with 24 transition metals ($x = 1/24$). The supercell volume was fixed to the one of a calculated, hypothetical empty P2-structure. Subsequently, we analysed the difference in energy between the respective site and the lowest energy site. Since only one sodium atom is placed within the large supercell, Na^+–Na^+ repulsion can be neglected and solely the influence of the immediate environment is modelled. Please note that these structures constitute a model system and do not reflect the experimentally found configurations (P2–O2 two-phase reaction).

For P2-$Na_xNi_{1/3}Mn_{2/3}O_2$, the honeycomb arrangement of the metal atoms distinguishes the Na_f sites in Na_f^{Mn-Mn} and Na_f^{Mn-Ni} that either sit in between two Mn octahedra (Mn–Na–Mn dumbbell) or in between a Ni and a Mn octahedra (Ni–Na–Mn dumbbell), respectively, while all Na_e are equivalent. In P2-$Na_{1/24}Ni_{1/3}Mn_{2/3}O_2$, the sodium site energies follow the trend $Na_e < Na_f^{Mn-Ni} < Na_f^{Mn-Mn}$ as presented in Fig. 9A. This qualitative trend can be rationalized when considering that the insertion of one Na atom leads to the reduction of one Ni centre

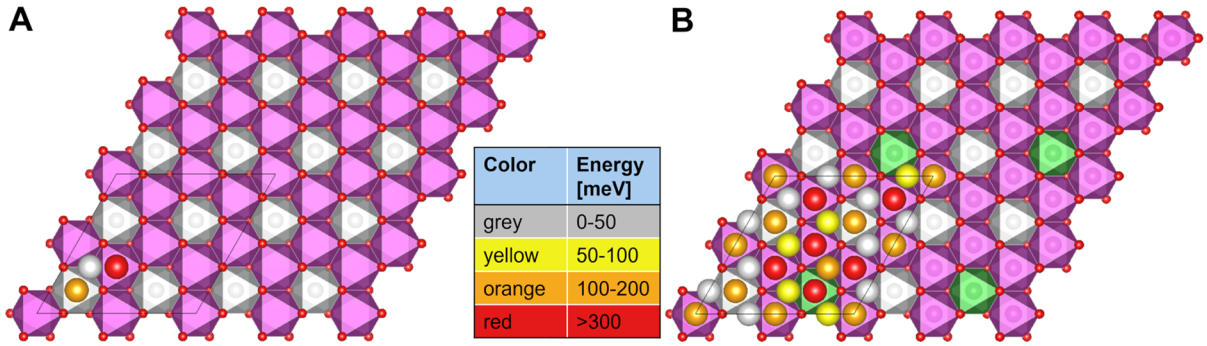

Fig. 9 Site energies for the high-vacancy limit corresponding to one Na atom per supercell in (A) P2-$Na_{1/24}Ni_{1/3}Mn_{2/3}O_2$ and in (B) P2-$Na_{1/24}Mn_{3/4}Ni_{1/4}O_2$. The Na atoms are coloured by an energy scale based on the site energy corresponding to the difference in energy of the respective site and the lowest energy site, where grey, yellow, orange and red correspond to the energy ranges 0–50 meV, 50–100 meV, 100–200 meV and >300 meV, respectively.

from Ni^{4+} to Ni^{3+}. Since the Na–O bond is ionic, Na^+ interacts with the charge density distribution in the MO_2 slab and Na sites in vicinity of Ni centres are beneficial due to their lower formal oxidation state. In P2-$Ni_{1/24}Mn_{3/4}Ni_{1/4}O_2$, the substitution of 1/12 of the Ni atoms by Mn atoms leads to further inequivalence of the Na sites when the nearest neighbour transition metals are considered, which is reflected in the sodium site energies as presented in Fig. 9B. The Na site energy is substantially increased for Na_f sites in Mn–Na–Mn dumbbells and the surrounding Na_e sites. This phenomenon is caused by the redox-inactive nature of the Mn atoms at such small sodium contents. Mn atoms remain in the formal 4+ oxidation state and therefore lead to significant electrostatic repulsion of the adjacent Na cations. The charge is compensated by a reduction of nearest-neighbour Ni atoms, which are considerably far from the particular high-energy sodium lattice sites. Overall, the calculated sodium site energies suggest preferential occupation of Na_e sites over Na_f sites in accordance with expectations based on Pauling's principles.[63] For P2-$Na_xNi_{1/3}Mn_{2/3}O_2$ (Fig. 9A), two energetically different Na_f sites are available, which arrange in a distinct pattern. For P2-$Ni_xMn_{3/4}Ni_{1/4}O_2$ (Fig. 9B), additional Mn–Na–Mn dumbbells result in an energy penalty for corresponding Na_f sites and adjacent Na_e sites. For P2-$Ni_xMn_{3/4}Ni_{1/4}O_2$, the simple site energy pattern, as observed for P2-$Na_xNi_{1/3}Mn_{2/3}O_2$, is disrupted. In this model experiment, site energies differ in more than 200 mV, suggesting a potentially strong influence of site energies on Na^+/vacancy orderings.

Encouraged by these results, we have analysed the most stable structures for $x = 2/3$, 1/2 and 1/3 in terms of charge ordering within the MO_2 slab and its relation to Na^+/vacancy ordering. Please note that the analysed structures are in accordance with the experimental characterization and therefore most likely resemble the physical reality. Respective structure files are provided in the ESI.† A depiction of the calculated most stable structures following the in-plane Na^+/vacancy orderings as reported by Lee *et al.*[46] is presented in Fig. 10A and B for P2-$Na_xNi_{1/3}Mn_{2/3}O_2$ and P2-$Ni_xMn_{3/4}Ni_{1/4}O_2$, respectively. For $x = 1/2$, an additional comparison between the Na^+/vacancy orderings reported by Lee *et al.*[46] and Huang *et al.*[83] is presented in ESI Fig. S16.† In both figures, the three-dimensional crystal structure is presented as stacking of three slices with [0 0 1] orientation. Charge ordering within the transition metal slab as derived from magnetic moments and Bader charges (Table 3) is depicted in the colour code. In-plane Na^+/vacancy orderings are presented in red colour for occupied Na_f sites and petrol colour for occupied Na_e sites (following the colour code in the publication by Lee *et al.*[46]). Occupied sodium sites are categorized by their closest neighbour transition metals and the respective oxidation state.

Orderings following Lee *et al.*[46] (Fig. 10) – for P2-$Na_xNi_{1/3}Mn_{2/3}O_2$, solely Ni^{2+} and Ni^{3+} next to Mn^{4+} are observed at $x = 2/3$ and 1/3, respectively, resulting in simple hexagonal charge orderings within the MO_2 slab. At $x = 1/2$, Ni^{2+} and Ni^{3+} arrange in alternating lines, which is in contrast to a more homogeneous charge distribution within the MO_2 slab following a hexagonal pattern. A similar charge ordering in lines has been observed for $Na_{1/2}CoO_2$.[83,95–97] For P2-$Ni_xMn_{3/4}Ni_{1/4}O_2$, the change in Ni/Mn stoichiometry leads to a shift to lower oxidation states as discussed above. At $x = 2/3$, the addition of manganese to the structure leads to two adjacent Mn^{3+} atoms. At $x = 1/2$, solely Ni^{2+} and Mn^{4+} is present. At $x = 1/3$, a line ordering of Ni^{3+} and Ni^{2+}/Mn^{4+} is observed. Overall, the simple charge orderings observed in P2-$Na_xNi_{1/3}Mn_{2/3}O_2$ are disrupted in P2-$Ni_xMn_{3/4}Ni_{1/4}O_2$. As a result of the simple charge orderings in P2-$Na_xNi_{1/3}Mn_{2/3}O_2$, Na_f sites are exclusively occupied if one of the nearest neighbour transition metals is Ni^{2+}. For each sodium stoichiometry, all occupied Na_e sites exhibit the same transition metal oxidation state environment. For P2-$Ni_xMn_{3/4}Ni_{1/4}O_2$, the disrupted charge ordering within the MO_2 slab causes more diverse nearest-neighbour environments for occupied Na_e and Na_f sites.

Ordering following Huang *et al.*[83] (ESI Fig. S16†) – for both P2-$Na_{1/2}Ni_{1/3}Mn_{2/3}O_2$ and P2-$Na_{1/2}Mn_{3/4}Ni_{1/4}O_2$, we find the same transition metal charge orderings for the in-plane Na^+/vacancy ordering reported by Huang *et al.*[83] and Lee *et al.*[46] Independent of the Ni/Mn ratio, two Na_f sites with different nearest-neighbour environments (Mn^{4+}–Na_f^+–Ni^{2+} and Mn^{4+}–Na_f^+–Mn^{4+}) and two energetically different Na_e sites are occupied. The nearest-neighbour environment of these Na_e sites is influenced by the Ni/Mn ratio, eventually influencing the stability of the Na^+/vacancy ordering.

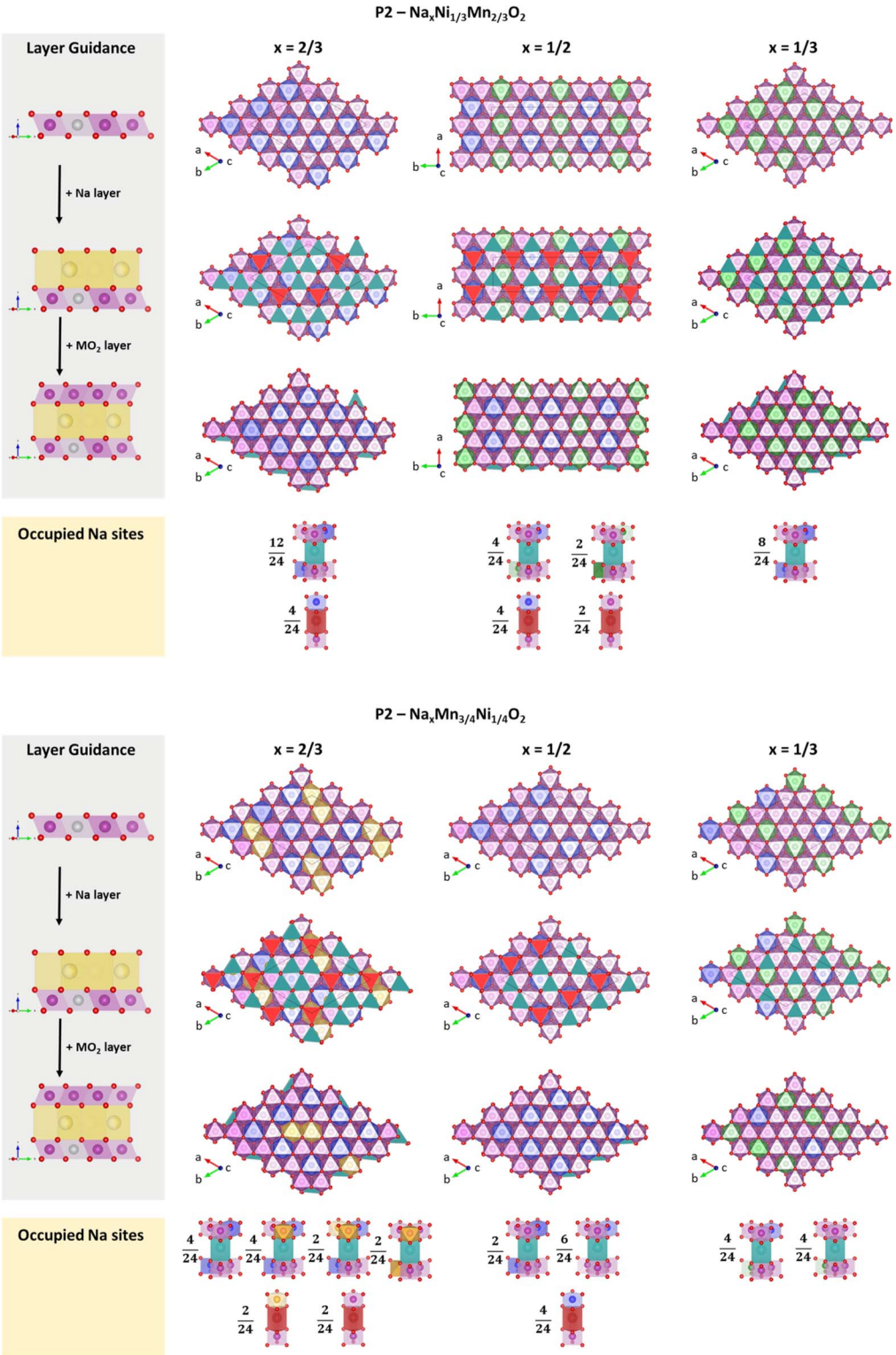

Fig. 10 Most stable structures following the in-plane Na^+/vacancy ordering reported by Lee *et al.*[46] in relation to the respective transition metal charge ordering for (A) P2-$Na_xNi_{1/3}Mn_{2/3}O_2$ and (B) P2-$Na_xMn_{3/4}Ni_{1/4}O_2$. Ni^{2+}, Ni^{3+}, Mn^{3+} and Mn^{4+} are presented in blue, green, yellow and magenta colour, respectively. Occupied Na_e sites are presented in petrol colour and Na_f sites are presented in red colour.

Comparison of evaluated Na^+/vacancy orderings at $x = 1/2$ – both *operando* XRD experiments and DFT calculations indicate that the Na^+/vacancy ordering as reported by Huang *et al.*[83] is present in P2-$Na_{1/2}Ni_{1/3}Mn_{2/3}O_2$. For P2-$Na_{1/2}Mn_{3/4}Ni_{1/4}O_2$, no indication for long-range Na^+/vacancy ordering is found in *operando* XRD experiments and DFT calculations suggest

a marginal energy benefit for the ordering reported by Lee *et al.*[46] Please note that the ordering reported by Huang *et al.*[83] incorporates a lower fraction of Na_e sites ($Na_e/Na_f = 1$) compared to the reported in-plane Na^+/vacancy ordering by Lee *et al.*[46] ($Na_e/Na_f = 2$). Furthermore, the ordering reported by Huang *et al.*[83] is characteristic for increased mean squared Na^+–Na^+ distances, resulting in an energy benefit by minimizing in-plane Na^+–Na^+ repulsion. For P2-$Na_{1/2}Ni_{1/3}Mn_{2/3}O_2$, the minimized Na^+–Na^+ repulsion (Huang ordering) seems to prevail over the effect of low energy sodium sites (Lee ordering). For P2-$Na_{1/2}Mn_{3/4}Ni_{1/4}O_2$, the disruption of the transition metal charge ordering destabilizes the ordering reported by Huang *et al.*[83] As a result, none of both Na^+/vacancy orderings results in a significant energy gain and long-range Na^+/vacancy ordering is disrupted.

Influence of Ni/Mn stoichiometry on Na^+/vacancy orderings – if we compare the same Na^+/vacancy ordered structure for P2-$Na_xNi_{1/3}Mn_{2/3}O_2$ and P2-$Na_xMn_{3/4}Ni_{1/4}O_2$ (vertical comparison in Fig. 10 and ESI fig. S16†), Na^+–Na^+ distances remain constant. Therefore, the relative stability of the compared Na^+/vacancy orderings is solely influenced by the transition metal environment. At $x = 2/3$, the decrease in the Ni/Mn ratio from P2-$Na_xNi_{1/3}Mn_{2/3}O_2$ to P2-$Na_xMn_{3/4}Ni_{1/4}O_2$ leads to the occupation of energetically more diverse sodium sites. Consequently, the Na^+/vacancy ordering is partially disrupted in P2-$Ni_xMn_{3/4}Ni_{1/4}O_2$. At $x = 1/2$, the transition metal charge ordering in rows in P2-$Na_xNi_{1/3}Mn_{2/3}O_2$ is disrupted when the Ni/Mn ratio is increased (P2-$Na_xMn_{3/4}Ni_{1/4}O_2$). As a result, the energy benefit of the Huang ordering is lost and any long-range Na^+/vacancy ordering is suppressed. At $x = 1/3$, no influence of the Ni/Mn ratio and the transition metal charge ordering on Na^+/vacancy ordering is found. Enabled by the relatively low sodium content, only low energy sodium sites are occupied in both materials and we conclude that Na^+/vacancy ordering at $x = 1/3$ is dominated by the effect of Na^+–Na^+ repulsion.

Guideline and discussion

Based on the above findings, we can deduce that the Na^+/vacancy orderings in P2-type Na_xMO_2 at sodium contents of $x = 2/3$ and 1/2 are considerably influenced by the charge ordering in the MO_2 slab. Therefore, these Na^+/vacancy orderings can be suppressed if the transition metal charge orderings are disrupted. The Na^+/vacancy ordering at $x = 1/3$ is dominated by Na^+–Na^+ repulsion and therefore is largely independent of charge ordering within the MO_2 slab.

To crosscheck this hypothesis, we have synthesized P2-$Na_{2/3}Ni_{1/4}Mg_{1/12}Mn_{2/3}O_2$ and P2-$Na_{3/4}Ni_{1/4}Li_{1/12}Mn_{2/3}O_2$. Within the applied potential range (1.5–4.3 V), Li^+ and Mg^{2+} remain redox inactive.[113–115] For P2-$Na_{2/3}Ni_{1/4}Mg_{1/12}Mn_{2/3}O_2$, the expected formal oxidation states (assuming Na^+ and O^{2-}) are $Na_{2/3}Ni_{1/4}{}^{II}Mg_{1/12}{}^{II}Mn_{2/3}{}^{IV}O_2$. According to Delmas *et al.*[58] the hexagonal transition metal ordering within the MO_2 slab results from the difference in ionic radii during synthesis. Based on the ionic radii (Ni^{2+} = 0.69 Å, Mg^{2+} = 0.72 Å, and Mn^{4+} = 0.53 Å),[116] we anticipate hexagonal ordering of small Mn^{4+} ions surrounding larger Ni^{2+} & Mg^{2+} ions. This honeycomb ordering is in accordance with literature reports.[51,60]

As a result, we expect the following formal oxidation states at $x = 2/3$, 1/2 and 1/3: $Na_{2/3}[Ni_{1/4}{}^{II}Mg_{1/12}{}^{II}]Mn_{2/3}{}^{IV}O_2$, $Na_{1/2}[Ni_{1/12}{}^{II}Ni_{2/12}{}^{III}Mg_{1/12}{}^{II}]Mn_{2/3}{}^{IV}O_2$ and $Na_{1/3}[Ni_{2/12}{}^{III}Ni_{1/12}{}^{IV}Mg_{1/12}{}^{II}]Mn_{2/3}{}^{IV}O_2$ ("C_1 site" in parenthesis). Therefore, a perfect honeycomb charge ordering is expected at $x = 2/3$, whereas a disrupted charge ordering is expected for $x = 1/2$ and 1/3. Following our guideline, we expect a potential jump caused by Na^+/vacancy ordering at $x = 2/3$ and a potential shoulder at $x = 1/2$. As discussed above, no effect of charge ordering on the Na^+/vacancy ordering at $x = 1/3$ is expected. The corresponding first cycle potential profile is presented in Fig. 11B. In accordance with literature reports,[51,113,117,118] the potential profile exhibits a distinct jump at $x = 2/3$ (approx. 3.0 V) and a smoothed jump at $x = 1/2$ (approx. 3.5 V). Similar to P2-$Na_{2/3}Ni_{1/3}Mn_{2/3}O_2$, the change from $Ni^{2+/3+}$ to $Mn^{3+/4+}$ redox most likely contributes to the significant voltage jump at $x = 2/3$.

For P2-$Na_{3/4}Ni_{1/4}{}^{II}Li_{1/12}{}^{I}Mn^{IV}{}_{2/3}O_2$, the expected formal oxidation states are $Na_{3/4}Ni_{1/4}{}^{II}Li_{1/12}{}^{I}Mn_{2/3}{}^{IV}O_2$, resulting in a hexagonal ordering of large Ni^{2+} & Li^+ (Li^+ = 0.76 Å)[116] surrounded by small Mn^{4+} within the MO_2 slab. In accordance with the literature,[113] superstructure reflections in the XRD pattern support the honeycomb superstructure within the MO_2 slab (ESI Fig. S17†). At the relevant sodium contents for Na^+/vacancy ordering, the corresponding formal oxidation states are $Na_{2/3}[Ni_{1/6}{}^{II}Ni_{1/12}{}^{III}Li_{1/12}{}^{I}]Mn_{2/3}{}^{IV}O_2$, $Na_{1/2}[Ni_{1/4}{}^{III}Li_{1/12}{}^{I}]Mn_{2/3}{}^{IV}O_2$ and $Na_{1/3}[Ni_{1/12}{}^{III}Ni_{1/6}{}^{IV}Li_{1/12}{}^{I}]Mn_{2/3}{}^{IV}O_2$. Following the guideline above, we expect highly disrupted charge ordering at $x = 2/3$, 1/2 and 1/3, leading to a considerably smooth potential profile for $x > 1/3$. The corresponding first cycle potential profile, as presented in Fig. 11C, is smooth and solely exhibits a small shoulder at $x = 2/3$ and a slight jump at $x = 1/3$ in accordance with earlier reports.[113,115,119] The significant voltage jump at $x = 3/4$ is most likely caused by the transition from $Ni^{2+/3+}$ to $Mn^{3+/4+}$ redox.

Further results, obtained by Al substitution for either Ni or Mn in P2-$Na_{2/3}Ni_{1/3}Mn_{2/3}O_2$, are presented in ESI Fig. S19.† Al substitution for Mn is expected to have only minor effects on the transition metal charge ordering in the MO_2 slab. Experimentally, we find no significant impact on the potential jumps indicative for Na^+/vacancy orderings at $x = 2/3$, 1/2 and 1/3. In contrast, Al substitution for Ni is expected to disrupt the transition metal charge ordering in the MO_2 slab. The experimentally found potential profile is significantly smoothened at $x = 2/3$ and 1/2 in accordance with earlier reports.[120]

The experimentally observed potential profiles for the undoped, Mg- and Li-doped samples (Fig. 11), as well as Al-substitutions (ESI Fig. S19†), comply with the expectations based on the herein postulated guideline, underlining the significant impact of transition metal charge ordering on Na^+/vacancy ordering. The cycling stability of the undoped, Mg- and Li-doped samples increases with decreasing tendency for Na^+/vacancy ordering (ESI Fig. S20†). Analogously to the above-discussed materials, the herein postulated guideline also holds for Zn-[113,121] and Cu-doping.[113,122–124]

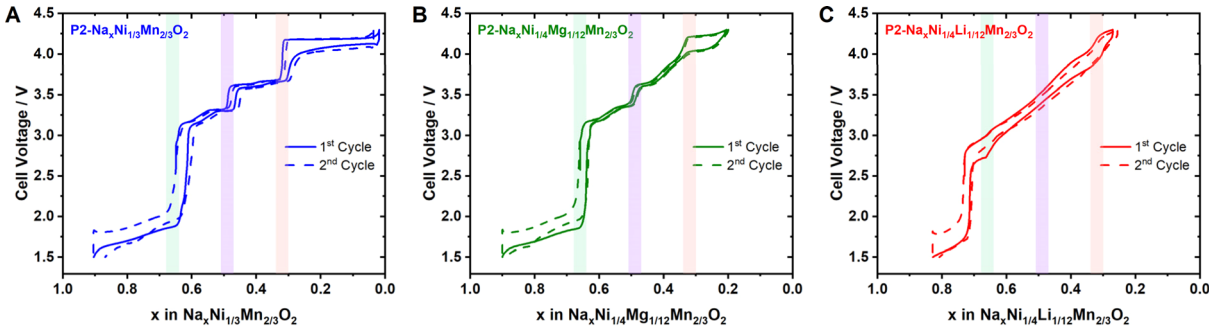

Fig. 11 Potential profile for the first two full galvanostatic cycles of (A) P2-$Na_{2/3}Ni_{1/3}Mn_{2/3}O_2$, (B) P2-$Na_{2/3}Ni_{1/4}Mg_{1/12}Mn_{2/3}O_2$ and (C) $Na_{3/4}Ni_{1/4}Li_{1/12}Mn_{2/3}O_2$ as cathode materials in a sodium half-cell.

High entropy materials – lately, "high entropy" materials are explored as promising future cathode materials.[125–130] Per definition, high entropy materials are single-phase materials consisting of at least five (near)-equimolar species, resulting in an ideal configurational entropy $S^{ideal} \geq 1.609\ k_B$ per transition metal site, where k_B is the Boltzmann constant.[125,131,132] In view of this work, the tendency for a smooth potential profile of "high entropy layered sodium transition metal oxides" can be rationalized. The presence of various transition metals with diverse formal oxidation states eliminates long-range charge ordering, which then results in suppressed Na^+/vacancy orderings and a smooth potential profile. Please note that high entropy cathode materials may exhibit further potential advantages, such as minimized strain or enhanced solid diffusion,[125,130,133–138] which are beyond the scope of this work.

Conclusion

Within this work, we have demonstrated the significance of charge ordering within the transition metal slab on the presence and extent of Na^+/vacancy orderings in P2-type cathode materials for sodium-ion batteries. Simple charge ordering patterns within the MO_2 slab support the tendency towards Na^+/vacancy orderings. Disrupted charge ordering patterns lead to disrupted or suppressed Na^+/vacancy orderings.

The herein proposed guideline enables the prediction of Na^+/vacancy orderings and the associated potential jumps solely on the transition metal composition, the consideration of formal oxidation states and well-known atomic crystal radii. In the first step, the presence of a honeycomb transition metal superstructure is analysed based on either experimental data or by considering the formal oxidation states and ionic radii of the transition metals in the as-synthesized material. In the second step, the formal oxidation states of the transition metals are calculated for sodium stoichiometries $x = 2/3$, 1/2 and 1/3. Combining the structural information (*e.g.*, honeycomb superstructure ordering within the MO_2 slab) with the formal oxidation states enables the prediction of charge ordering and, as a consequence, the tendency for Na^+/vacancy ordering.

Besides estimating the tendency for detrimental Na^+/vacancy orderings in a given transition metal composition, this rather simple framework can as well serve to design and optimize cathode compositions with suppressed Na^+/vacancy orderings and therefore improved long-term cycling stability.

Data availability

Experimental data, including diffraction data and electrochemical data, are publicly available *via* the zenodo repository at **https://doi.org/10.5281/zenodo.13911290**. The complete computational data sets are available *via* the NOMAD repository at **https://doi.org/10.17172/NOMAD/2024.10.10-2**.

Author contributions

L. F. P. – writing original draft, conceptualization, formal analysis, methodology, visualization. M. D. – writing original draft, conceptualization, formal analysis, methodology, visualization. N. B. – investigation, software, formal analysis, methodology. P. B. – formal analysis, software. D. R. – investigation, formal analysis. M. Z. – investigation, data curation. P. D. – investigation. C. H. – investigation. D. M. – investigation, data curation. A. O. – investigation, data curation. V. B. – investigation, resources. N. P. – resources, formal analysis. M. S. – investigation, formal analysis, visualization. M. B. – investigation, formal analysis, methodology. M. W. M. – supervision, funding acquisition, methodology. A. G. – supervision, funding acquisition. S. P. – supervision, project administration, funding acquisition. P. A. – supervision, project administration, funding acquisition. All authors reviewed and edited the manuscript.

Conflicts of interest

There are no conflicts to declare.

Acknowledgements

This work was funded by the German Federal Ministry of Education and Research (BMBF) in the projects TRANSITION (03XP0186C, 03XP0186A), transition transfer (03XP0533A, 03XP0533B) and ExcellBattMat (03XP0257A, 03XP0257C and 03XP0254D) and by the German Research Foundation (DFG) in the project POLIS Cluster of Excellence (ProjectID 390874152). Computational resources have been provided by the state of

Baden-Wuerttemberg through bwHPC and the German Research Foundation (DFG) through Grant No. INST 40/575-1 FUGG (JUSTUS 2 cluster). Neutron diffraction measurements were carried out at the CANAM infrastructure of the NPI CAS Rez using the CICRR infrastructure supported by MEYS project LM2023041, both of which are acknowledged. We acknowledge DESY (Hamburg, Germany), a member of the Helmholtz Association HGF, for the provision of experimental facilities. Parts of this research were carried out at the P02.1 beamline. The authors thank Gisela Arnold (ZSW) for ICP-OES analysis and Wolfgang Weirather (ZSW) for precipitation of hydroxide precursors.

References

1 IPCC, *Climate Change 2023: Synthesis Report. Contribution of Working Groups I, II and III to the Sixth Assessment Report of the Intergovernmental Panel on Climate Change, Geneva, Switzerland*, ed. Core Writing Team, H. Lee and J. Romero, 2023, p. 184, DOI: **10.59327/IPCC/AR6-9789291691647**.
2 S. Passerini, L. Barelli, M. Baumann, J. Peters and M. Weil, *Emerging Battery Technologies to Boost the Clean Energy Transition*, Springer International Publishing, Cham, 2024.
3 T. M. Gür, *Energy Environ. Sci.*, 2018, **11**, 2696–2767.
4 B. Dunn, H. Kamath and J.-M. Tarascon, *Science*, 2011, **334**, 928–935.
5 M. Armand, P. Axmann, D. Bresser, M. Copley, K. Edström, C. Ekberg, D. Guyomard, B. Lestriez, P. Novák, M. Petranikova, W. Porcher, S. Trabesinger, M. Wohlfahrt-Mehrens and H. Zhang, *J. Power Sources*, 2020, **479**, 228708.
6 European Commission, *Directorate General for Internal Market, Industry, Entrepreneurship and SMEs., Study on the Critical Raw Materials for the EU 2023: Final Report*, Publications Office, 2023.
7 L. Boer, A. Pescatori and M. Stuermer, *Discussion Papers 1976*, 2021, **https://www.diw.de/de/diw_01.c.826751.de/publikationen/diskussionspapiere/2021_1976/energy_transition_metals.html**.
8 International Energy Agency (IEA), *The Role of Critical Minerals in Clean Energy Transitions, World Energy Outlook Special Report*, 2021.
9 D. Gielen, *Critical Materials for the Energy Transition*, International Renewable Energy Agency, [Abu Dhabi], 2021.
10 N. Tapia-Ruiz, A. R. Armstrong, H. Alptekin, M. A. Amores, H. Au, J. Barker, R. Boston, W. R. Brant, J. M. Brittain, Y. Chen, M. Chhowalla, Y.-S. Choi, S. I. R. Costa, M. C. Ribadeneyra, S. A. Cussen, E. J. Cussen, W. I. F. David, A. V. Desai, S. A. M. Dickson, E. I. Eweka, J. D. Forero-Saboya, C. P. Grey, J. M. Griffin, P. Gross, X. Hua, J. T. S. Irvine, P. Johansson, M. O. Jones, M. Karlsmo, E. Kendrick, E. Kim, O. V. Kolosov, Z. Li, S. F. L. Mertens, R. Mogensen, L. Monconduit, R. E. Morris, A. J. Naylor, S. Nikman, C. A. O'Keefe, D. M. C. Ould, R. G. Palgrave, P. Poizot, A. Ponrouch, S. Renault, E. M. Reynolds, A. Rudola, R. Sayers, D. O. Scanlon, S. Sen, V. R. Seymour, B. Silván, M. Tahar Sougrati, L. Stievano, G. S. Stone, C. I. Thomas, M.-M. Titirici, J. Tong, T. J. Wood, D. S. Wright and R. Younesi, *JPhys Energy*, 2021, **3**, 31503, DOI: **10.1088/2515-7655/ac01ef**.
11 A. Rudola, A. J. R. Rennie, R. Heap, S. S. Meysami, A. Lowbridge, F. Mazzali, R. Sayers, C. J. Wright and J. Barker, *J. Mater. Chem. A*, 2021, **9**, 8279–8302.
12 A. Bauer, J. Song, S. Vail, W. Pan, J. Barker and Y. Lu, *Adv. Energy Mater.*, 2018, **8**, 1702869, DOI: **10.1002/aenm.201702869**.
13 Y.-S. Hu and Y. Li, *ACS Energy Lett.*, 2021, **6**, 4115–4117.
14 Y.-K. Sun, *ACS Energy Lett.*, 2020, **5**, 1278–1280.
15 J.-M. Tarascon, *Joule*, 2020, **4**, 1616–1620, **https://www.sciencedirect.com/science/article/pii/S2542435120302403**.
16 *Sodium-Ion Batteries*, ed. M.-M. Titirici, P. Adelhelm and Y.-S. Hu, Wiley, 2022.
17 F. Xie, Z. Xu, Z. Guo and M.-M. Titirici, *Prog. Energy*, 2020, **2**, 42002.
18 H. Moon, A. Innocenti, H. Liu, H. Zhang, M. Weil, M. Zarrabeitia and S. Passerini, *ChemSusChem*, 2023, **16**, e202201713.
19 H. Moon, M. Zarrabeitia, E. Frank, O. Böse, M. Enterría, D. Saurel, I. Hasa and S. Passerini, *Batteries Supercaps*, 2021, **4**, 960–977.
20 M. Thompson, Q. Xia, Z. Hu and X. S. Zhao, *Mater. Adv.*, 2021, **2**, 5881–5905.
21 D. Larcher and J.-M. Tarascon, *Nat. Chem.*, 2015, **7**, 19–29, **https://www.nature.com/articles/nchem.2085#change-history**.
22 C. Vaalma, D. Buchholz, M. Weil and S. Passerini, *Nat. Rev. Mater.*, 2018, **3**, 1–11, **https://www.nature.com/articles/natrevmats201813**.
23 K. Kubota, M. Dahbi, T. Hosaka, S. Kumakura and S. Komaba, *Chem. Rec.*, 2018, **18**, 459–479.
24 K. Kubota and S. Komaba, *J. Electrochem. Soc.*, 2015, **162**, A2538–A2550.
25 I. Hasa, S. Mariyappan, D. Saurel, P. Adelhelm, A. Y. Koposov, C. Masquelier, L. Croguennec and M. Casas-Cabanas, *J. Power Sources*, 2021, **482**, 228872, **https://www.sciencedirect.com/science/article/pii/S0378775320311769**.
26 W. Zuo, A. Innocenti, M. Zarrabeitia, D. Bresser, Y. Yang and S. Passerini, *Acc. Chem. Res.*, 2023, **56**, 284–296.
27 J. F. Peters, M. Baumann, J. R. Binder and M. Weil, *Sustainable Energy Fuels*, 2021, **5**, 6414–6429.
28 J. Peters, M. Baumann, M. Weil and S. Passerini, in *Sodium-Ion Batteries*, ed. M.-M. Titirici, P. Adelhelm and Y.-S. Hu, Wiley, 2022, vol. 24, pp. 551–571.
29 F. B. Jasper, J. Späthe, M. Baumann, J. F. Peters, J. Ruhland and M. Weil, *J. Cleaner Prod.*, 2022, **366**, 132899.
30 J. Peters, A. Peña Cruz and M. Weil, *Batteries*, 2019, **5**, 10.
31 A. Rudola, C. J. Wright and J. Barker, *Energy Mater. Adv.*, 2021, **2021**, 37.
32 S. Kuze, J.-i. Kageura, S. Matsumoto, T. Nakayama, M. Makidera, M. Saka, T. Yamaguchi, T. Yamamoto and

K. Nakane, *Development of a Sodium Ion Secondary Battery, R&D Report*, 2013.
33 Q. Zhou, Y. Li, F. Tang, K. Li, X. Rong, Y. Lu, L. Chen and Y.-S. Hu, *Chin. Phys. Lett.*, 2021, **38**, 76501.
34 E. Gonzalo, M. Zarrabeitia, N. E. Drewett, L. del Amo, J. Miguel and T. Rojo, *Energy Storage Mater.*, 2021, **34**, 682–707, https://www.sciencedirect.com/science/article/pii/S2405829720303883.
35 E. Goikolea, V. Palomares, S. Wang, I. R. de Larramendi, X. Guo, G. Wang and T. Rojo, *Adv. Energy Mater.*, 2020, **10**, 2002055, DOI: 10.1002/aenm.202002055.
36 N. Ortiz-Vitoriano, N. E. Drewett, E. Gonzalo and T. Rojo, *Energy Environ. Sci.*, 2017, **10**, 1051–1074, https://pubs.rsc.org/en/content/articlelanding/2017/ee/c7ee00566k.
37 C. Delmas, C. Fouassier and P. Hagenmuller, *Physica B+C*, 1980, **99**, 81–85, https://www.sciencedirect.com/science/article/pii/0378436380902144.
38 S. P. Ong, V. L. Chevrier, G. Hautier, A. Jain, C. Moore, S. Kim, X. Ma and G. Ceder, *Energy Environ. Sci.*, 2011, **4**, 3680.
39 A. van der Ven, G. Ceder, M. Asta and P. D. Tepesch, *Phys. Rev. B: Condens. Matter Mater. Phys.*, 2001, **64**, 16.
40 Y. Mo, S. P. Ong and G. Ceder, *Chem. Mater.*, 2014, **26**, 5208–5214.
41 P. Gupta, S. Pushpakanth, M. A. Haider and S. Basu, *ACS Omega*, 2022, **7**(7), 5605–5614.
42 J. Zhang, W. Wang, W. Wang, S. Wang and B. Li, *ACS Appl. Mater. Interfaces*, 2019, **11**, 22051–22066.
43 J. M. Paulsen and J. R. Dahn, *Solid State Ionics*, 1999, **126**, 3–24.
44 Z. Lu and J. R. Dahn, *Chem. Mater.*, 2001, **148**, A1225.
45 Z. Lu and J. R. Dahn, *Chem. Mater.*, 2001, **13**, 1252–1257.
46 D. H. Lee, J. Xu and Y. S. Meng, *Phys. Chem. Chem. Phys.*, 2013, **15**, 3304–3312.
47 R. J. Clément, P. G. Bruce and C. P. Grey, *J. Electrochem. Soc.*, 2015, **162**, A2589, DOI: 10.1149/2.0201514jes.
48 S. Daubner, M. Dillenz, L. F. Pfeiffer, C. Gauckler, M. Rosin, N. Burgard, J. Martin, P. Axmann, M. Sotoudeh, A. Gross, D. Schneider and B. Nestler, *npj Comput. Mater.*, 2024, **10**, 1020.
49 J. Mao, X. Liu, J. Liu, H. Jiang, T. Zhang, G. Shao, G. Ai, W. Mao, Y. Feng, W. Yang, G. Liu and K. Dai, *J. Electrochem. Soc.*, 2019, **166**, A3980–A3986.
50 T. Risthaus, D. Zhou, X. Cao, X. He, B. Qiu, J. Wang, L. Zhang, Z. Liu, E. Paillard, G. Schumacher, M. Winter and J. Li, *J. Power Sources*, 2018, **395**, 16–24.
51 N. Tapia-Ruiz, W. M. Dose, N. Sharma, H. Chen, J. Heath, J. W. Somerville, U. Maitra, M. S. Islam and P. G. Bruce, *Energy Environ. Sci.*, 2018, **11**, 1470–1479.
52 L. Lu, X. Han, J. Li, J. Hua and M. Ouyang, *J. Power Sources*, 2013, **226**, 272–288.
53 C. Gauckler, M. Dillenz, F. Maroni, L. F. Pfeiffer, J. Biskupek, M. Sotoudeh, Q. Fu, U. Kaiser, S. Dsoke, H. Euchner, P. Axmann, M. Wohlfahrt-Mehrens, A. Groß and M. Marinaro, *ACS Appl. Energy Mater.*, 2022, **5**, 13735–13750.
54 A. Gutierrez, W. M. Dose, O. Borkiewicz, F. Guo, M. Avdeev, S. Kim, T. T. Fister, Y. Ren, J. Bareño and C. S. Johnson, *J. Phys. Chem. C*, 2018, **122**, 23251–23260.
55 P. Manikandan, D. Ramasubramonian and M. M. Shaijumon, *Electrochim. Acta*, 2016, **206**, 199–206.
56 L. F. Pfeiffer, N. Jobst, C. Gauckler, M. Lindén, M. Marinaro, S. Passerini, M. Wohlfahrt-Mehrens and P. Axmann, *Front. Energy Res.*, 2022, **10**, 305.
57 L. F. Pfeiffer, Y. Li, M. Mundszinger, J. Geisler, C. Pfeifer, D. Mikhailova, A. Omar, V. Baran, J. Biskupek, U. Kaiser, P. Adelhelm, M. Wohlfahrt-Mehrens, S. Passerini and P. Axmann, *Chem. Mater.*, 2023, **35**, 8065–8080.
58 C. Delmas, D. Carlier and M. Guignard, *Adv. Energy Mater.*, 2021, **11**, 2001201.
59 B. L. Henke, E. M. Gullikson and J. C. Davis, *At. Data Nucl. Data Tables*, 1993, **54**, 181–342.
60 J. M. Paulsen, R. A. Donaberger and J. R. Dahn, *Chem. Mater.*, 2000, **12**, 2257–2267.
61 J. M. Paulsen and J. R. Dahn, *J. Electrochem. Soc.*, 2000, **147**, 2478.
62 R. Balsys, *Solid State Ionics*, 1997, **93**, 279–282.
63 L. Pauling, *J. Am. Chem. Soc.*, 1929, **51**, 1010–1026.
64 V. F. Sears, *Neutron News*, 1992, vol. 3, pp. 26–37.
65 J. W. Somerville, A. Sobkowiak, N. Tapia-Ruiz, J. Billaud, J. G. Lozano, R. A. House, L. C. Gallington, T. Ericsson, L. Häggström, M. R. Roberts, U. Maitra and P. G. Bruce, *Energy Environ. Sci.*, 2019, **12**, 2223–2232.
66 J. Rodríguez-Carvajal, *Phys. B*, 1993, **192**, 55–69.
67 M. Casas-Cabanas, M. Reynaud, J. Rikarte, P. Horbach and J. Rodríguez-Carvajal, *J. Appl. Crystallogr.*, 2016, **49**, 2259–2269.
68 K. Momma and F. Izumi, *J. Appl. Crystallogr.*, 2011, **44**, 1272–1276.
69 A.-C. Dippel, H.-P. Liermann, J. T. Delitz, P. Walter, H. Schulte-Schrepping, O. H. Seeck and H. Franz, *J. Synchrotron Radiat.*, 2015, **22**, 675–687.
70 J. Filik, A. W. Ashton, P. C. Y. Chang, P. A. Chater, S. J. Day, M. Drakopoulos, M. W. Gerring, M. L. Hart, O. V. Magdysyuk, S. Michalik, A. Smith, C. C. Tang, N. J. Terrill, M. T. Wharmby and H. Wilhelm, *J. Appl. Crystallogr.*, 2017, **50**, 959–966.
71 M. Herklotz, J. Weiß, E. Ahrens, M. Yavuz, L. Mereacre, N. Kiziltas-Yavuz, C. Dräger, H. Ehrenberg, J. Eckert, F. Fauth, L. Giebeler and M. Knapp, *J. Appl. Crystallogr.*, 2016, **49**, 340–345.
72 P. Hohenberg and W. Kohn, *Phys. Rev.*, 1964, **136**, B864–B871.
73 W. Kohn and L. J. Sham, *Phys. Rev.*, 1965, **140**, A1133–A1138.
74 P. E. Blöchl, *Phys. Rev. B: Condens. Matter Mater. Phys.*, 1994, **50**, 17953–17979.
75 J. P. Perdew, K. Burke and M. Ernzerhof, *Phys. Rev. Lett.*, 1996, **77**, 3865–3868.
76 S. Grimme, S. Ehrlich and L. Goerigk, *J. Comput. Chem.*, 2011, **32**, 1456–1465.
77 G. Kresse and J. Furthmüller, *Phys. Rev. B: Condens. Matter Mater. Phys.*, 1996, **54**, 11169–11186.

78 G. Kresse and J. Hafner, *Phys. Rev. B: Condens. Matter Mater. Phys.*, 1993, **47**, 558–561.
79 G. Kresse and D. Joubert, *Phys. Rev. B: Condens. Matter Mater. Phys.*, 1999, **59**, 1758–1775.
80 S. L. Dudarev, G. A. Botton, S. Y. Savrasov, C. J. Humphreys and A. P. Sutton, *Phys. Rev. B: Condens. Matter Mater. Phys.*, 1998, **57**, 1505–1509.
81 A. Jain, S. P. Ong, G. Hautier, W. Chen, W. D. Richards, S. Dacek, S. Cholia, D. Gunter, D. Skinner, G. Ceder and K. A. Persson, *APL Mater.*, 2013, **1**, 1049.
82 L. Wang, T. Maxisch and G. Ceder, *Am. Mineral.*, 2006, **73**, 603.
83 Q. Huang, M. L. Foo, J. W. Lynn, H. W. Zandbergen, G. Lawes, Y. Wang, B. H. Toby, A. P. Ramirez, N. P. Ong and R. J. Cava, *J. Solid State Chem.*, 2004, **16**, 5803–5814.
84 P. P. Ewald, *Ann. Phys.*, 1921, **369**, 253–287.
85 S. P. Ong, W. D. Richards, A. Jain, G. Hautier, M. Kocher, S. Cholia, D. Gunter, V. L. Chevrier, K. A. Persson and G. Ceder, *Comput. Mater. Sci.*, 2013, **68**, 314–319.
86 W. Zuo, J. Qiu, X. Liu, F. Ren, H. Liu, H. He, C. Luo, J. Li, G. F. Ortiz, H. Duan, J. Liu, M.-S. Wang, Y. Li, R. Fu and Y. Yang, *Nat. Commun.*, 2020, **11**, 3544.
87 W. Zuo, Z. Xiao, M. Zarrabeitia, X. Xue, Y. Yang and S. Passerini, *ACS Mater. Lett.*, 2022, **4**, 1074–1086.
88 H. Xia, L. Lu, Y. S. Meng and G. Ceder, *J. Power Sources*, 2007, **154**, A337.
89 L. W. Shacklette, T. R. Jow and L. Townsend, *J. Electrochem. Soc.*, 1988, **135**, 2669–2674.
90 R. Berthelot, D. Carlier and C. Delmas, *Nat. Mater.*, 2011, **10**, 74–80.
91 H. W. Zandbergen, M. Foo, Q. Xu, V. Kumar and R. J. Cava, *Solid State Ionics*, 2004, **70**, 431.
92 D. Igarashi, Y. Miyazaki, T. Kajitani and K. Yubuta, *Phys. Rev. B: Condens. Matter Mater. Phys.*, 2008, **78**, 235.
93 Y. Reynier, J. Graetz, T. Swan-Wood, P. Rez, R. Yazami and B. Fultz, *Phys. Rev. B: Condens. Matter Mater. Phys.*, 2004, **70**, 753.
94 M. Blangero, R. Decourt, D. Carlier, G. Ceder, M. Pollet, J.-P. Doumerc, J. Darriet and C. Delmas, *Inorg. Chem.*, 2005, **44**, 9299–9304.
95 Q. Huang, M. L. Foo, R. A. Pascal, J. W. Lynn, B. H. Toby, T. He, H. W. Zandbergen and R. J. Cava, *Phys. Rev. B: Condens. Matter Mater. Phys.*, 2004, **70**, 453.
96 P. Zhang, R. B. Capaz, M. L. Cohen and S. G. Louie, *Phys. Rev. B: Condens. Matter Mater. Phys.*, 2005, **71**, 165.
97 M. L. Foo, Y. Wang, S. Watauchi, H. W. Zandbergen, T. He, R. J. Cava and N. P. Ong, *Phys. Rev. Lett.*, 2004, **92**, 247001.
98 Y. S. Meng, Y. Hinuma and G. Ceder, *J. Chem. Phys.*, 2008, **128**, 104708.
99 Y. Hinuma, Y. S. Meng and G. Ceder, *Solid State Ionics*, 2008, **77**, 165.
100 H. Alloul, I. R. Mukhamedshin, T. A. Platova and A. V. Dooglav, *Europhys. Lett.*, 2009, **85**, 47006.
101 T. A. Platova, I. R. Mukhamedshin, H. Alloul, A. V. Dooglav and G. Collin, *Phys. Rev. B: Condens. Matter Mater. Phys.*, 2009, **80**, 224106.
102 R. A. Huggins, Advanced Batteries, *Materials Science Aspects*, Springer US, Boston, MA, 2009.
103 P. de Silva and C. Corminboeuf, *J. Chem. Theory Comput.*, 2014, **10**, 3745–3756.
104 M. Busch, R. B. Wang, A. Hellman, J. Rossmeisl and H. Grönbeck, *J. Phys. Chem. C*, 2018, **122**, 216–226.
105 A. Visibile, R. B. Wang, A. Vertova, S. Rondinini, A. Minguzzi, E. Ahlberg and M. Busch, *Chem. Mater.*, 2019, **31**, 4787–4792.
106 C. Elschenbroich, *Organometallchemie*, Teubner, Wiesbaden, 5th edn, 2005.
107 A. F. Holleman, N. Wiberg and E. Wiberg, *Lehrbuch der Anorganischen Chemie*, Walter de Gruyter, 2007.
108 M. Busch, E. Ahlberg and I. Panas, *Phys. Chem. Chem. Phys.*, 2011, **13**, 15069–15076.
109 A. Visibile, A. Vertova, S. Rondinini, A. Minguzzi, E. Ahlberg and M. Busch, *Chem. Phys. Lett.*, 2020, **755**, 137799.
110 I. R. Mukhamedshin and H. Alloul, *Phys. B*, 2015, **460**, 58–63.
111 X. Chen, Y. Wang, K. Wiaderek, X. Sang, O. Borkiewicz, K. Chapman, J. LeBeau, J. Lynn and X. Li, *Adv. Funct. Mater.*, 2018, **28**, 385.
112 X. Li, X. Ma, D. Su, L. Liu, R. Chisnell, S. P. Ong, H. Chen, A. Toumar, J.-C. Idrobo, Y. Lei, J. Bai, F. Wang, J. W. Lynn, Y. S. Lee and G. Ceder, *Nat. Mater.*, 2014, **13**, 586–592.
113 Y. Li, K. A. Mazzio, N. Yaqoob, Y. Sun, A. I. Freytag, D. Wong, C. Schulz, V. Baran, A. S. J. Mendez, G. Schuck, M. Zając, P. Kaghazchi and P. Adelhelm, *Adv. Mater.*, 2024, e2309842.
114 R. A. House, U. Maitra, L. Jin, J. G. Lozano, J. W. Somerville, N. H. Rees, A. J. Naylor, L. C. Duda, F. Massel, A. V. Chadwick, S. Ramos, D. M. Pickup, D. E. McNally, X. Lu, T. Schmitt, M. R. Roberts and P. G. Bruce, *Chem. Mater.*, 2019, **31**, 3293–3300.
115 R. J. Clément, J. Xu, D. S. Middlemiss, J. Alvarado, C. Ma, Y. S. Meng and C. P. Grey, *J. Mater. Chem. A*, 2017, **5**, 4129–4143.
116 R. D. Shannon, *Acta Crystallogr.*, 1976, **32**, 751–767.
117 H. Hou, B. Gan, Y. Gong, N. Chen and C. Sun, *Inorg. Chem.*, 2016, **55**, 9033–9037.
118 P.-F. Wang, Y. You, Y.-X. Yin, Y.-S. Wang, L.-J. Wan, L. Gu and Y.-G. Guo, *Angew. Chem., Int. Ed. Engl.*, 2016, **55**, 7445–7449.
119 J. Xu, D. H. Lee, R. J. Clément, X. Yu, M. Leskes, A. J. Pell, G. Pintacuda, X.-Q. Yang, C. P. Grey and Y. S. Meng, *Chem. Mater.*, 2014, **26**, 1260–1269.
120 I. Hasa, S. Passerini and J. Hassoun, *J. Mater. Chem. A*, 2017, **5**, 4467–4477.
121 X. Wu, G.-L. Xu, G. Zhong, Z. Gong, M. J. McDonald, S. Zheng, R. Fu, Z. Chen, K. Amine and Y. Yang, *ACS Appl. Mater. Interfaces*, 2016, **8**, 22227–22237.
122 K. Kubota, Y. Yoda and S. Komaba, *J. Electrochem. Soc.*, 2017, **164**, A2368, DOI: **10.1149/2.0311712jes**.
123 L. Wang, Y.-G. Sun, L.-L. Hu, J.-Y. Piao, J. Guo, A. Manthiram, J. Ma and A.-M. Cao, *J. Mater. Chem. A*, 2017, **5**, 8752–8761.

124 L. Zheng, J. Li and M. N. Obrovac, *Chem. Mater.*, 2017, **29**, 1623–1631.
125 B. Ouyang and Y. Zeng, *Nat. Commun.*, 2024, **15**, 973.
126 A. Sarkar, L. Velasco, D. Wang, Q. Wang, G. Talasila, L. de Biasi, C. Kübel, T. Brezesinski, S. S. Bhattacharya, H. Hahn and B. Breitung, *Nat. Commun.*, 2018, **9**, 3400.
127 F. Strauss, M. Botros, B. Breitung and T. Brezesinski, *J. Appl. Phys.*, 2024, **135**, 420.
128 R. Guo, Y. Yang, C. Zhao, F. Huo, J. Xue, J. He, B. Sun, Z. Sun, H. K. Liu and S. X. Dou, *Adv. Funct. Mater.*, 2023, **19**, 2022.
129 Y. Ma, Y. Ma, Q. Wang, S. Schweidler, M. Botros, T. Fu, H. Hahn, T. Brezesinski and B. Breitung, *Energy Environ. Sci.*, 2021, **14**, 2883–2905.
130 B. Wang, J. Ma, K. Wang, D. Wang, G. Xu, X. Wang, Z. Hu, C. -W. Pao, J. -L. Chen, L. Du, X. Du and G. Cui, *Adv. Energy Mater.*, 2024, **35**, 38.
131 E. P. George, D. Raabe and R. O. Ritchie, *Nat. Rev. Mater.*, 2019, **4**, 515–534.
132 J. -W. Yeh, S. -K. Chen, S. -J. Lin, J. -Y. Gan, T. -S. Chin, T. -T. Shun, C. -H. Tsau and S. -Y. Chang, *Adv. Eng. Mater.*, 2004, **6**, 299–303.
133 F. Ding, C. Zhao, D. Xiao, X. Rong, H. Wang, Y. Li, Y. Yang, Y. Lu and Y.-S. Hu, *J. Am. Chem. Soc.*, 2022, **144**, 8286–8295.
134 S. L. Dreyer, R. Zhang, J. Wang, A. Kondrakov, Q. Wang, T. Brezesinski and J. Janek, *JPhys Energy*, 2023, **5**, 35002.
135 J. Liu, W. Huang, R. Liu, J. Lang, Y. Li, T. Liu, K. Amine and H. Li, *Adv. Funct. Mater.*, 2024, **34**, 2315437.
136 K. Tian, H. He, X. Li, D. Wang, Z. Wang, R. Zheng, H. Sun, Y. Liu and Q. Wang, *J. Mater. Chem. A*, 2022, **10**, 14943–14953.
137 J. Wang, S. L. Dreyer, K. Wang, Z. Ding, T. Diemant, G. Karkera, Y. Ma, A. Sarkar, B. Zhou, M. V. Gorbunov, A. Omar, D. Mikhailova, V. Presser, M. Fichtner, H. Hahn, T. Brezesinski, B. Breitung and Q. Wang, *Mater. Futures*, 2022, **1**, 35104.
138 C. Zhao, F. Ding, Y. Lu, L. Chen and Y.-S. Hu, *Angew. Chem., Int. Ed. Engl.*, 2020, **59**, 264–269.

